Geophys. J. Int. (2025) **xxx**, **??–??**

Numerical wavefield simulations with instantaneous time mirror in a 3D elastic medium

V. Kurapati[1*], G. Hillers[2], L. Krenz[1], A.-A. Gabriel[3,4], M. Bader[1]

∗ *corresponding author,*
[1] *TUM School of Computation, Information and Technology, Technical University of Munich, Munich, Germany*
[2] *Institute of Seismology, Department of Geosciences and Geography, University of Helsinki, Helsinki, Finland*
[3] *Scripps Institution of Oceanography, University of San Diego, San Diego California, USA*
[4] *Department of Earth and Environmental Sciences, Ludwig-Maximilians-University of Munich, Munich, Germany*

Received 202x month day; in original form 202x month day 22

SUMMARY

We model elastic wave propagation in time-varying media with a focus on wave behavior at a time interface and an instantaneous time mirror (ITM) using analytical solutions and numerical experiments. We develop an eigenvector-based analytical solution for time interfaces for general linear hyperbolic wave systems and apply it to analyze the energy balance at time boundaries and ITMs. The energy increases for all intermittent medium changes, for all impedance scaling factors smaller and larger than unity. The analytical solutions provide a reference for our numerical convergence tests that show a high order convergence which demonstrates the effectiveness of the employed SeisSol ADER-DG numerical solution. Its accuracy is corroborated by estimates of reflection and transmission coefficients and observed frequency shifts across time boundaries, and by acoustic wave speed estimates obtained from focal spots associated with ITM generated converging P waves that are consistent with theoretical predictions and ground truth values, respectively. We use the new SeisSol ITM feature to simulate the partitioning of seismic body waves excited by a point force in a spatially homogeneous elastic full space. The response to an intermittent short change in the elastic parameters yields a diverging and converging P and S wavefield. A systematic scaling of the elastic parameters is then used to steer independent ITM reflections of either P or S wave components. Numerical ITM solutions as developed here can be used to synthesize converging wavefields in seismic imaging applications, and more generally to analyze the behavior and manipulation of seismic wavefields in space-time varying media.

Key words: Seismic Waves; Elastic Waves; Body Waves; Acoustic Waves; Time-Reversal; Spacetime Transformation; Instantaneous Time Mirror; Refocusing; Impedance Contrast; ADER-DG

1 INTRODUCTION

Space and time play equivalently important roles in wave propagation (Wapenaar et al., 2024). Thus, understanding the effects of space-varying *and* time-varying material properties on the wavefield is essential for many applications. For seismic waves propagating in Earth, the impedance contrasts associated with layer boundaries and material changes (Fig. 1a) lead to well-studied phenomena that are important for our understanding of Earth structure. The space-time analogy (Fig. 1b) implies that reflections can also be caused by an interface or a disruption of material properties in time (Wapenaar et al., 2024). Intermittent, short-duration changes of the impedance-governing medium properties can lead to an instantaneous time mirror (ITM) (Bacot et al., 2016; Fink & Fort, 2017), which creates time-boundary reflections by activating "sources" everywhere in space (Fig. 1c).

Understanding the complex effects of space-time wavefield variations is essential for the manipulation of wavefields. ITM sources localized in time excite divergent and convergent waves just as material contrasts in space act as localized sources for

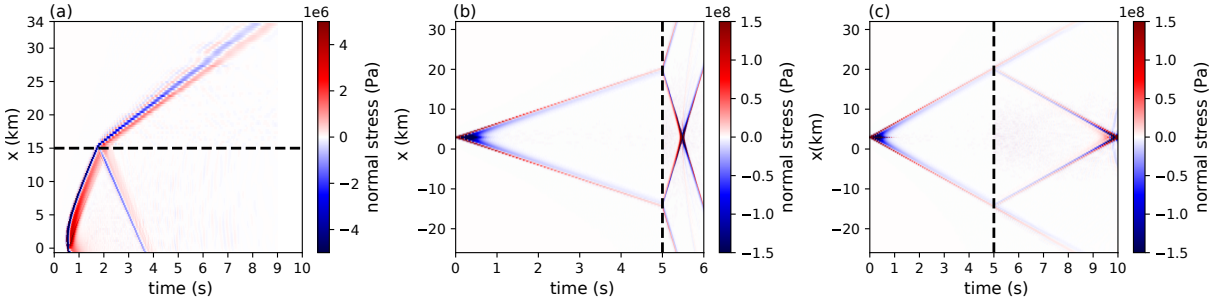

Figure 1. Space-time representations of simulated acoustic wavefields. All panels show the normal stress or pressure along the x-axis in response to a pressure impulse moment tensor point source. In each panel the source and receiver configuration is adapted to demonstrate the responses. The dashed lines indicate the space and time interfaces. (a) Reflection and transmission at an impedance contrast or interface in space. (b) Reflection and transmission at a single impedance contrast or interface in time. (c) Reflection and transmission at an instantaneous time mirror ITM. The ITM consists of two time interfaces separated by a very short interval τ.

transmitted and reflected waves (Fig. 1). Convergent waves excited by the ITM and by a classic time-reversal mirror (Fink, 1997) demonstrate the time-reversal invariance property of the wave equation. However, in contrast to the functioning of a time-reversal mirror (Fink & Fort, 2017) that records, stores, time-reverses, and re-transmits a wave signal, the ITM does not involve an antenna of receiver-transmitter elements.

Bacot et al. (2016) developed a framework for explaining ITM effects that are based on the wave speed-dependent coupling of the wavefield amplitude to its time derivative. A temporal wave speed disruption decouples the amplitude and its derivative and forms a new set of initial conditions that are controlled by the wavefield state in the entire medium at the instant of the mirror activation. This leads to a superposition of two decomposed states corresponding to the forward-propagating and backward-propagating waves. This manipulation retains a first in-last out symmetry (Fig. 1c) and thus differs from the reflections at boundaries in space (Fig. 1a) and at a time-reversal mirror with their first-in-first-out sequence. Bacot et al. (2016) first demonstrated the wave speed-dependent ITM principle experimentally by disrupting the propagation of gravity water waves through an instantaneous acceleration, which intermittently changes the wave propagation speed in the medium due to its dependence on gravitational acceleration. Since then, time-dependent properties of various materials in different spectral bands have been manipulated to focus, shape, and control the propagation of electromagnetic (Pacheco-Peña & Engheta, 2020; Wu et al., 2022; Tirole et al., 2023; Galiffi et al., 2023), acoustic (Gérardin et al., 2019), and elastic waves (Innanen, 2018).

The seismic wavefield anatomy can be controlled by manipulating active source properties, and specific source-receiver configurations can enhance target signals. In contrast, seismic metamaterials (Colombi et al., 2016; Mu et al., 2020) can passively influence the properties of an incident wavefield. A regular spatial configuration of resonators, including buildings (Guéguen et al., 2002), pile walls (Dijckmans et al., 2016), trenches (Pu & Shi, 2020), inclusions (Castanheira-Pinto et al., 2018), wind turbines (Pilz et al., 2024), and trees (Roux et al., 2018) can control the local wavefield, which has important implications for structural engineering, urban planning, seismic safety, and hazard mitigation. Simulated time-reversed seismic wavefields are used for earthquake source characterization (Rietbrock & Scherbaum, 1994; Larmat et al., 2006), and simulations are an essential element in adjoint imaging techniques for solving tomographic inverse problems (Tromp et al., 2005). The analogy between time-reversal and cross-correlation (Derode et al., 2003) explains the reconstruction of converging and diverging waves (Shapiro et al., 2005; Lin et al., 2009; Gallot et al., 2011) and of spatial autocorrelation fields (Ekström et al., 2009; Hillers et al., 2016) from correlations of continuous seismic dense array records for passive surface wave imaging.

Reflectors in space and mirrors in time have been studied for wavefields in a range of materials (Catheline et al., 2008). The water wave example demonstrated by Peng et al. (2020) showed that a change in the parameters that control the wave speed creates a time slab or ITM. The properties of the propagation media in the solid Earth and its envelopes, including the hydrosphere, cryosphere, and atmosphere, can experience sudden changes associated with natural and anthropogenic phenomena such as earthquakes, eruptions, collapses, explosions, and injections. However, except for the numerical study of propagation in a 2D elastic medium by Innanen (2018), the ITM response of a 3D elastic or seismic wavefield is not analyzed comprehensively.

In this work, we extend the numerical wave propagation code SeisSol (Käser et al., 2010; Käser & Dumbser, 2006;

Dumbser & Käser, 2006; Dumbser et al., 2007a; Krenz et al., 2023; Gabriel et al., 2025) with an implementation of ITM physics in elastic media to study the effects of spacetime transformation on seismic wavefields. SeisSol has demonstrated its utility and performance in modeling earthquake scenarios with several billion degrees of freedom while achieving a significant fraction of the theoretical peak performance (Heinecke et al., 2014; Uphoff et al., 2017; Krenz et al., 2021). Our ITM implementation extends SeisSol's versatility to analyze a broader range of acoustic and elastic wave propagation phenomena (Fig. 1). We use SeisSol to manipulate the propagation of P waves and S waves simultaneously or separately, providing a tool and a basis for further investigations of seismic ITM effects.

In the next Section 2 we discuss the general wave equation and plane wave solutions using eigenvectors, introduce an analytical solution for the ITM disruption of an acoustic wave, and discuss ITM physics for the elastic wave equation. We demonstrate the ITM implementation for the elastic case in SeisSol and perform a numerical convergence test in Section 3. In Section 4 we report the results from point source simulations for the acoustic case and the elastic case, before we discuss the implications for applications in Section 5.

2 PLANE WAVE SOLUTIONS IN RESPONSE TO TIME INTERFACES

2.1 Plane wave solution for the general wave equation with a time interface

In this work, a time interface activated at t_{int} shall be a step-function change in the material properties with respect to the previous state, and the intermittently activated instantaneous time mirror discussed in Sections 2.2 to 4 is a short sequence of two opposite step-function changes. This excludes more general time variations such as continuous, periodic, or other transient components (Wapenaar et al., 2024). We consider a general linear hyperbolic wave equation expressed in the first-order form

$$\frac{\partial \mathbf{q}}{\partial t} + \mathbf{A}\frac{\partial \mathbf{q}}{\partial x} + \mathbf{B}\frac{\partial \mathbf{q}}{\partial y} + \mathbf{C}\frac{\partial \mathbf{q}}{\partial z} = 0, \tag{1}$$

where the state vector $\mathbf{q}$ depends on time t and spatial directions x, y, z. The flux matrices in x, y, z are given by $\mathbf{A}, \mathbf{B}, \mathbf{C}$. Solutions to this system of constant-coefficient linear partial different equations (PDEs) can be expressed as a linear summation of planar waves, similar to a Fourier basis decomposition (Sec. 4.2.1 in Evans, 2010). Using complex numbers, a plane wave with angular frequency ω and wavenumber k propagating in direction $\mathbf{n}$ can be written as

$$\mathbf{q}\left(\mathbf{x}, t\right) = \mathbf{r}\, e^{i(\omega t - k\mathbf{n}\cdot\mathbf{x})}, \tag{2}$$

with $\mathbf{x} = (x, y, z)$ and $\mathbf{n} = (n_1, n_2, n_3)$ the unit vector that denotes the direction of propagation. Inserting eq. (2) into eq. (1), we obtain that the state vector $\mathbf{q}\left(\mathbf{x}, t\right)$ solves eq. (1) if

$$\underbrace{\left(\mathbf{A}n_1 + \mathbf{B}n_2 + \mathbf{C}n_3\right)}_{\hat{\mathbf{A}}}\mathbf{r} = \frac{\omega}{k}\mathbf{r}. \tag{3}$$

Thus, $\mathbf{r}$ needs to be an eigenvector of the plane wave operator $\hat{\mathbf{A}}$, where the wave speed $c = \omega/k$ is the corresponding eigenvalue. To formulate general solutions of the PDE system in eq. (1), we express the initial condition $\mathbf{q}\left(\mathbf{x}, 0\right)$ as a linear sum of eigenvectors with space-dependent functions, setting $t = 0$ in eq. (2)

$$\mathbf{q}\left(\mathbf{x}, 0\right) = \sum_j \mathbf{r}_j f_j\left(\mathbf{n}\cdot\mathbf{x}\right) = \sum_j \mathbf{r}_j e^{i(-k_j\mathbf{n}\cdot\mathbf{x})}, \quad f_j\left(\mathbf{n}\cdot\mathbf{x}\right) := e^{i(-k_j\mathbf{n}\cdot\mathbf{x})}, \tag{4}$$

where $\mathbf{r}_j$ is the jth eigenvector and f_j is the component of the jth eigenvector in the linear split (LeVeque, 2002, Sec. 18.5). The plane wave solution of the PDE system in eq. (1) is then

$$\mathbf{q}\left(\mathbf{x}, t\right) = \sum_j \mathbf{r}_j f_j\left(\mathbf{n}\cdot\mathbf{x} - c_j t\right) = \sum_j \mathbf{r}_j e^{i(\omega_j t - k_j\mathbf{n}\cdot\mathbf{x})}, \tag{5}$$

where c_j is the jth eigenvalue, corresponding to the wave velocity.

The following discussion examines the plane wave solution with a single time-interface. We distinguish two cases associated with constant and with changing eigenvectors, respectively. This can be related to the acoustic scenarios discussed in Sections 9.7 and 9.8 in LeVeque (2002), where an invariant or a changing impedance between two domains with different wave speed and density are associated with a constant or varying eigenvector interface, respectively. The first invariant impedance interface is associated with a tuned scenario where the wave speeds and densities differ but their product does not.

2.1.1 Eigenvectors do not change at the time interface

If the eigenvectors do not change at the time interface t_{int}, the new set of initial conditions is

$$\mathbf{q}\left(\mathbf{x}, t_{\text{int}}\right) = \sum_j \mathbf{r_j} f_j\left(\mathbf{n}\cdot\mathbf{x} - c_j t_{\text{int}}\right) = \sum_j \mathbf{r}_j e^{i\left(\omega_j t_{\text{int}} - k_j \mathbf{n}\cdot\mathbf{x}\right)}, \tag{6}$$

which evolves in time according to

$$\mathbf{q}\left(\mathbf{x}, t\right) = \sum_j \mathbf{r_j} f_j\left(\mathbf{n}\cdot\mathbf{x} - c_j t_{\text{int}} - \hat{c}_j(t - t_{\text{int}})\right) = \sum_j \mathbf{r}_j e^{i\left(\hat{\omega}_j(t - t_{\text{int}}) + \omega_j t_{\text{int}} - k\mathbf{n}\cdot\mathbf{x}\right)}. \tag{7}$$

Here, $\mathbf{r_j}$ is the jth eigenvector, f_j is the component of the jth eigenvector in the linear split, and c_j is the jth eigenvalue. Correspondingly, $\hat{c}_j$ and $\hat{\omega}_j = k_j \hat{c}_j$ are the jth eigenvalue and the jth angular frequency after the material change, respectively. In this scenario, the wave components associated with different eigenvectors propagate without creating new components. However, their velocities can change if the eigenvalues vary, which results in a phase shift.

2.1.2 Eigenvectors change at the time interface

If, on the other hand, the eigenvectors change in response to the material change at the time interface t_{int}, we split the new initial conditions

$$\mathbf{q}\left(\mathbf{x}, t_{\text{int}}\right) = \sum_j \mathbf{r_j} f_j\left(\mathbf{n}\cdot\mathbf{x} - c_j t_{\text{int}}\right) = \sum_i \hat{\mathbf{r}}_\mathbf{j} \hat{f}_j\left(\mathbf{n}\cdot\mathbf{x}\right), \tag{8}$$

which evolves in time as

$$\mathbf{q}\left(\mathbf{x}, t\right) = \sum_j \hat{\mathbf{r}}_\mathbf{j} \hat{f}_j\left(\mathbf{n}\cdot\mathbf{x} - \hat{c}_j(t - t_{\text{int}})\right), \tag{9}$$

where $\hat{\mathbf{r}}_j$ denotes the jth eigenvector after the material change, $\hat{f}_j$ denotes the space-dependent component of the jth eigenvector, and $\hat{c}_j$ denotes the jth eigenvalue.

This shows that there can be components of different eigenvectors and eigenvalue pairs associated with the time interface. If, after the time interface, the decomposition of the new initial conditions creates eigenvectors that have eigenvalues such that they exist in $\pm$ pairs, it results in a reflected component in time. Hence if eigenvalues exist only in pairs of negative and positive values, reflections can be caused with a time interface. This is the case for the set of elastic wave equations analyzed in Section 2.3.

If we consider a system with eigenvalues c and $-c$ and eigenvectors $\mathbf{r_1}$ and $\mathbf{r_2}$, the solution after the time interface, i.e., the forward component, even if we begin with only one component, is

$$\mathbf{q}\left(\mathbf{x}, t_{\text{int}}\right) = \mathbf{r_1} f_1\left(\mathbf{n}\cdot\mathbf{x} - c t_{\text{int}}\right) = \hat{\mathbf{r}}_\mathbf{1} \hat{f}_1\left(\mathbf{n}\cdot\mathbf{x}\right) + \hat{\mathbf{r}}_\mathbf{2} \hat{f}_2\left(\mathbf{n}\cdot\mathbf{x}\right), \tag{10}$$

which evolves in time as

$$\mathbf{q}\left(\mathbf{x}, t\right) = \hat{\mathbf{r}}_\mathbf{1} \hat{f}_1\left(\mathbf{n}\cdot\mathbf{x} - \hat{c}\left(t - t_{\text{int}}\right)\right) + \hat{\mathbf{r}}_\mathbf{2} \hat{f}_2\left(\mathbf{n}\cdot\mathbf{x} + \hat{c}\left(t - t_{\text{int}}\right)\right), \tag{11}$$

i.e., a single component creates its reflection. Here $\hat{\mathbf{r}}_\mathbf{i}$ is the eigenvector after the time interface, $\hat{f}_i$ is the component of the eigenvector $\hat{\mathbf{r}}_\mathbf{i}$, and $\hat{c}$ is the eigenvalue of the solution after the time interface. In a scenario where the eigenvectors can be manipulated to affect only one component of the solution without modifying the other, only one component of the wavefield is reflected. This scenario is explored here by manipulating elastic P waves and S waves independently.

If the initial eigenvalues are c_1 and c_2 with the corresponding eigenvalues $\hat{c}_1$ and $\hat{c}_2$ we obtain a solution that is similar to the result associated with a single initial eigenvector

$$\mathbf{q}\left(\mathbf{x}, t_{\text{int}}\right) = \mathbf{r_1} f_1\left(\mathbf{n}\cdot\mathbf{x} - c_1 t_{\text{int}}\right) = \hat{\mathbf{r}}_\mathbf{1} \hat{f}_i\left(\mathbf{n}\cdot\mathbf{x}\right) + \hat{\mathbf{r}}_\mathbf{2} \hat{f}_2\left(\mathbf{n}\cdot\mathbf{x}\right), \tag{12}$$

$$\mathbf{q}\left(\mathbf{x}, t\right) = \hat{\mathbf{r}}_\mathbf{1} \hat{f}_i\left(\mathbf{n}\cdot\mathbf{x} - \hat{c}_1\left(t - t_{\text{int}}\right)\right) + \hat{\mathbf{r}}_\mathbf{2} \hat{f}_2\left(\mathbf{n}\cdot\mathbf{x} - \hat{c}_2\left(t - t_{\text{int}}\right)\right). \tag{13}$$

This result demonstrates that this combination of eigenvalues does not necessarily create a reflected component. In our analysis, we focus on scenarios where the eigenvectors do change, since we are interested in obtaining reflections and in time reversing.

2.2 Analytical solution for an acoustic plane wave in response to time interfaces and the energy balance

Next, we discuss the analytical solution for an acoustic planar wavefield in response to a single time interface and an instantaneous time mirror (ITM). Bacot et al. (2016) defines an ITM as a sequence of time interfaces where the wave properties are changed intermittently for a very short duration τ. A corresponding analytical development for the elastic case is beyond the scope of this paper. As in Section 2.1, we work with a sinusoidal plane wave model. The set of acoustic wave equations in first-order hyperbolic form are defined as

$$\begin{aligned} \frac{\partial p}{\partial t} + \lambda \frac{\partial v_i}{\partial x_i} &= 0 \\ \rho \frac{\partial v_i}{\partial t} + \frac{\partial p}{\partial x_i} &= 0, \end{aligned} \tag{14}$$

where p is the pressure fluctuation, v_i are the particle velocities in the three directions, λ is the bulk modulus, and ρ is the density. The sound wave speed in the acoustic medium is $c = \sqrt{\lambda/\rho}$. We next describe ITM-generated converging wavefield components in an acoustic 1D system. We formulate eq. (14) in 1D and analogous to eq. (1) as

$$\frac{\partial \mathbf{q}}{\partial t} + \mathbf{A}\frac{\partial \mathbf{q}}{\partial x} = 0 \qquad \text{or} \qquad \frac{\partial}{\partial t}\begin{pmatrix} p \\ v \end{pmatrix} + \begin{pmatrix} 0 & \lambda \\ \frac{1}{\rho} & 0 \end{pmatrix} \frac{\partial}{\partial x}\begin{pmatrix} p \\ u \end{pmatrix} = 0. \tag{15}$$

The eigenvalues for this system $c = \pm\sqrt{\lambda/\rho}$ exist in pairs and the eigenmatrix

$$\mathbf{R} = \begin{pmatrix} -\sqrt{\rho\lambda} & \sqrt{\rho\lambda} \\ 1 & 1 \end{pmatrix} \tag{16}$$

depends only on the material parameters λ and ρ. In the following discussion, subscripts I, II, and III denote the three phases of the ITM system. Phase I denotes the time before the first time interface, phase II refers to the interval between the first and the second time interface, and phase III indicates the state after the second time interface.

2.2.1 Phase I

The expression of the forward propagating wave

$$\begin{aligned} p_{\mathrm{I}}(x,t) &= \rho c \cos\left(k\left(x - ct\right)\right), \\ v_{\mathrm{I}}(x,t) &= \cos\left(k\left(x - ct\right)\right), \end{aligned} \tag{17}$$

solves the 1D acoustic wave equation (eq. 15), where p_{I} and v_{I} denote the pressure and velocity evolution before the first time interface. Again, k is the wavenumber of the propagating wave, the sound speed is $c = \sqrt{\lambda/\rho}$ and the wave propagates in a medium with an initial impedance $Z_{\mathrm{I}} = \rho c$. The energy of the system is defined in a periodic domain following Kopriva et al. (2021):

$$E = \int_{-\frac{\pi}{k}}^{\frac{\pi}{k}} \left(\frac{1}{2\lambda}p^2 + \frac{1}{2}\rho v^2\right) dx. \tag{18}$$

For the initial conditions we obtain

$$E_{\mathrm{I}} = \frac{\pi\rho}{k}, \tag{19}$$

where E_{I} is again the energy of the system before the activation of the time interface. Energy as defined in eq. (18) is conserved for a system of conserved hyperbolic equations, if no external energy or force acts on it. For our analysis, this energy remains constant until the system properties change at a time interface, and the energy remains constant between time interfaces.

2.2.2 Phase II

An impedance contrast or interface in space causes a reflection of the wave (Sec. 9.2 in LeVeque, 2002) (Fig. 1a). To create a time interface, we scale the wave impedance by a factor of n when the ITM is activated. At $t = t_{\mathrm{ITM}}^{-}$ the Lamé parameter is changed to $\lambda_2 = n^2\lambda$, which changes the impedance to $Z_2 = nZ_1$. The solution to the correspondingly updated eq. (15) is

(LeVeque, 2002, Sec. 2.8)

$$\begin{aligned}\frac{2p_{\mathrm{II}}\left(x,t\right)}{c\rho} &= -\left(n-1\right)\cos\left(kx+cknt-\left(ckn+ck\right)t_{\mathrm{ITM}}^{-}\right)\\ &\quad+\left(n+1\right)\cos\left(kx-cknt+\left(ckn-ck\right)t_{\mathrm{ITM}}^{-}\right),\\ 2v_{\mathrm{II}}\left(x,t\right) &= \left(n-1\right)\cos\left(kx+cknt-\left(ckn+ck\right)t_{\mathrm{ITM}}^{-}\right)\\ &\quad+\left(n+1\right)\cos\left(kx-cknt+\left(ckn-ck\right)t_{\mathrm{ITM}}^{-}\right),\end{aligned} \tag{20}$$

where p_{II} and v_{II} are the pressure and velocity for $t > t_{\mathrm{ITM}}^{-}$. In each of the two pressure and velocity components, the first and second term correspond to a converging and diverging part of the solution, respectively. For this choice of material change, the forward and backward propagating waves travel with a speed of nc, i.e., the wave speed is multiplied by n. These solutions also indicate a phase shift of $\left(ckn \mp ck\right)t_{\mathrm{ITM}}^{-}$ for a wave propagating forward and backward in response to the time interface, respectively, which is consistent with the observations and conclusions of Bacot et al. (2016). Using eq. (18) we can evaluate the system energy at $t > t_{\mathrm{ITM}}^{-}$ to

$$E_{\mathrm{II}} = \frac{1}{2}\frac{\left(1+n^2\right)\pi\rho}{kn^2}. \tag{21}$$

Fig. 2(a) evaluates the energy ratio $E_{\mathrm{II}}/E_{\mathrm{I}}$ for different values of the time impedance factor n. Compared to the E_{I} reference state, the relative energy in the jolted system E_{II} decreases from large values at small $n < 1$ towards the asymptotic value of 0.5 for $n > 1$.

2.2.3 Phase III

At $t = t_{\mathrm{ITM}}^{+}$ we change the material properties back to their initial state and solve eq. (15) again, which yields

$$\begin{aligned}\frac{-4np_{\mathrm{III}}\left(x,t\right)}{c\rho} &= \left(-n^2+1\right)\cos\left(kx+ckt-2\,ckt_{\mathrm{ITM}}^{-}-\left(ckn+ck\right)\tau\right)\\ &\quad+\left(n^2-1\right)\cos\left(kx+ckt-2\,ckt_{\mathrm{ITM}}^{-}+\left(ckn-ck\right)\tau\right)\\ &\quad+\left(n^2-2n+1\right)\cos\left(kx-ckt+\left(ckn+ck\right)\tau\right)\\ &\quad+\left(-n^2-2n-1\right)\cos\left(kx-ckt-\left(ckn-ck\right)\tau\right),\\ -4nv_{\mathrm{III}}\left(x,t\right) &= \left(n^2-1\right)\cos\left(kx+ckt-2\,ckt_{\mathrm{ITM}}^{-}-\left(ckn+ck\right)\tau\right)\\ &\quad+\left(-n^2+1\right)\cos\left(kx+ckt-2\,ckt_{\mathrm{ITM}}^{-}+\left(ckn-ck\right)\tau\right)\\ &\quad+\left(n^2-2n+1\right)\cos\left(kx-ckt+\left(ckn+ck\right)\tau\right)\\ &\quad+\left(-n^2-2n-1\right)\cos\left(kx-ckt-\left(ckn-ck\right)\tau\right),\end{aligned} \tag{22}$$

where $\tau = t_{\mathrm{ITM}}^{+} - t_{\mathrm{ITM}}^{-}$, and p_{III} and v_{III} are pressure and velocity for $t > t_{\mathrm{ITM}}^{+}$, respectively. Eq. (22) consists of four components, two components each traveling in the forward and reverse directions. This shows that an impedance discontinuity in time or an ITM generates a time-reversed wave component. The wave components exhibit a phase shift that depends on the ITM parameters. The final energy E_{III} depends on the parameters k, n, and τ and is constrained by

$$\frac{\pi\rho}{k} \le E_{\mathrm{III}} \le \frac{\pi\rho}{2k}\left(n^2+\frac{1}{n^2}\right). \tag{23}$$

This demonstrates that the application of an ITM leads to a change in the system energy. We can compare the maximum energy increase after the ITM to the initial state. We take the upper limit expression and plot the ratio $E_{\mathrm{III}}/E_{\mathrm{I}}$ as a function of n. The minimum neutral value $E_{\mathrm{III}}/E_{\mathrm{I}} = 1$ is obtained at $n = 1$, and the system behavior is therefore consistent with the observation by Bacot et al. (2016) that "a temporal discontinuity in a homogeneous medium conserves momentum but not energy".

2.3 The elastic wave equation

In Section 2.1, we have established the association between paired positive and negative eigenvalues and a time-reflected propagating plane wave in the presence of time interfaces using a general solution of a first-order wave equation. Next, we demonstrate this principle for an elastic medium to provide a basis for evaluating our numerical results that involve manipula-

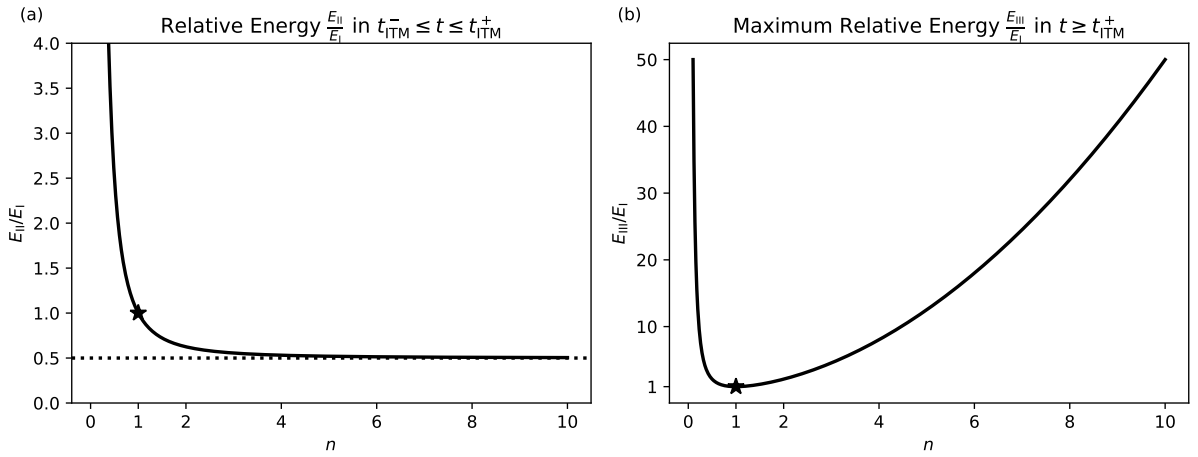

Figure 2. Energy ratios associated with time interfaces. The subscript I refers to the original state before the activation of a time interface, and states II and III are associated with the first and second time interface, respectively. The corresponding equations for $E_{\rm I}$, $E_{\rm II}$, and $E_{\rm III}$ are eqs (19), (21), and (23), respectively, and n is the wave impedance factor. The ratio (a) $E_{\rm II}/E_{\rm I}$. The dashed line indicates the asymptotic value of 0.5. (b) The ratio $E_{\rm III}/E_{\rm I}$. The star indicates the neutral state associated with $n = 1$.

tion of P waves and S waves. To model the 3D seismic wavefield, we use the velocity-stress formulation of the elastic wave equation. Using Einstein notation to indicate summation over repeated indices, these equations are

$$\begin{aligned} \frac{\partial \sigma_{ij}}{\partial t} - \lambda \delta_{ij} \frac{\partial v_k}{\partial x_k} - \mu \left(\frac{\partial v_i}{\partial x_j} + \frac{\partial v_j}{\partial x_i} \right) = 0, \\ \rho \frac{\partial v_i}{\partial t} - \frac{\partial \sigma_{ij}}{\partial x_j} = 0, \end{aligned} \tag{24}$$

where $\boldsymbol{\sigma}$ is the stress tensor, and consistent with eq. (14) the v_1, v_2, and v_3 are again the particle velocities in the x, y, and z directions, respectively, λ and μ are the material dependent Lamé parameters, and ρ is density. The acoustic wave equation (eq. 14) emerges as a special case of eq. (24) for $\mu = 0$. In this case, all shear stresses $\sigma_{ij} = 0$ vanish, and all normal stresses are equal and equivalent to the pressure fluctuation $p = -\sigma_{ii}$. Eq. (24) matches the general linear PDE system eq. (1)

$$\frac{\partial \mathbf{q}}{\partial t} + \mathbf{A}\frac{\partial \mathbf{q}}{\partial x} + \mathbf{B}\frac{\partial \mathbf{q}}{\partial y} + \mathbf{C}\frac{\partial \mathbf{q}}{\partial z} = 0$$

for the state vector

$$\mathbf{q} = \left(\sigma_{11},\, \sigma_{22},\, \sigma_{33},\, \sigma_{12},\, \sigma_{23},\, \sigma_{31},\, v_1,\, v_2,\, v_3\right)^T. \tag{25}$$

The flux matrices $\mathbf{A}$, $\mathbf{B}$, and $\mathbf{C}$ are 9×9 matrices, e.g.,

$$\mathbf{A} = \begin{pmatrix} 0 & 0 & 0 & 0 & 0 & 0 & -(\lambda+2\mu) & 0 & 0 \\ 0 & 0 & 0 & 0 & 0 & 0 & -\lambda & 0 & 0 \\ 0 & 0 & 0 & 0 & 0 & 0 & -\lambda & 0 & 0 \\ 0 & 0 & 0 & 0 & 0 & 0 & 0 & -\mu & 0 \\ 0 & 0 & 0 & 0 & 0 & 0 & 0 & 0 & 0 \\ 0 & 0 & 0 & 0 & 0 & 0 & 0 & 0 & -\mu \\ -\frac{1}{\rho} & 0 & 0 & 0 & 0 & 0 & 0 & 0 & 0 \\ 0 & 0 & 0 & -\frac{1}{\rho} & 0 & 0 & 0 & 0 & 0 \\ 0 & 0 & 0 & 0 & 0 & -\frac{1}{\rho} & 0 & 0 & 0 \end{pmatrix}. \tag{26}$$

We refer to Dumbser & Käser (2006) for the organization of these elements in the flux matrices, and for $\mathbf{B}$ and $\mathbf{C}$. The eigenvalues of this system $(-c_p, -c_s, -c_s, 0, 0, 0, c_s, c_s, c_p)$ determine the propagation velocities of P waves and S waves,

$c_p = \sqrt{(\lambda + 2\mu)/\rho}$ and $c_s = \sqrt{\mu/\rho}$, respectively. The corresponding eigenvector matrix is (Dumbser & Käser, 2006)

$$\mathbf{R} = \begin{pmatrix} \rho c_p & 0 & 0 & 0 & 0 & 0 & 0 & 0 & \rho c_p \\ \frac{\lambda}{c_p} & 0 & 0 & 0 & 1 & 0 & 0 & 0 & \frac{\lambda}{c_p} \\ \frac{\lambda}{c_p} & 0 & 0 & 0 & 0 & 1 & 0 & 0 & \frac{\lambda}{c_p} \\ 0 & \rho c_s & 0 & 0 & 0 & 0 & 0 & \rho c_s & 0 \\ 0 & 0 & 0 & 1 & 0 & 0 & 0 & 0 & 0 \\ 0 & 0 & \rho c_s & 0 & 0 & 0 & \rho c_s & 0 & 0 \\ 1 & 0 & 0 & 0 & 0 & 0 & 0 & 0 & -1 \\ 0 & 1 & 0 & 0 & 0 & 0 & 0 & -1 & 0 \\ 0 & 0 & 1 & 0 & 0 & 0 & -1 & 0 & 0 \end{pmatrix}. \tag{27}$$

The eigenvector matrix depends on the elastic material parameters ρ, λ, and μ. This means that a material change at a time interface can create a situation in which the new eigenvectors differ compared to the eigenvectors before the time interface. Following the discussion in Section 2.1.2 we infer that the eigenvalues occur in pairs $\pm c_p$, $\pm c_s$, $\pm c_s$, and the zero eigenvalues do not contribute to propagating waves. Hence a material interface that leads to a change in the eigenvectors leads to a corresponding reflected wavefield component.

This interaction of waves with material interfaces is a fundamental and well-studied aspect of wave propagation in general and seismic responses in particular (LeVeque, 2002, Sec. 9.2). These findings can be generalized to understand the wavefield response to time interfaces, which also exhibits splitting the propagation into time-reflected and transmitted components (Fig. 1b). As said, extending the single time interface to a time slab or instantaneous time mirror involves the restoration to the original medium parameters, i.e., the phase I and phase III medium properties are the same (Section 2.2), which leads to the same wave speeds before and after the ITM as in the water tank experiment by Bacot et al. (2016). The development of the 3D analytical ITM solutions for elastic waves excited by point or seismic sources is an interesting problem that we do not pursue.

3 WAVEFIELD SIMULATIONS AND ITM IMPLEMENTATION IN SEISSOL

In this section, we summarize the implementation details of wavefield simulations with SeisSol and highlight the necessary modifications associated with the physics of time interfaces.

3.1 Overview of ADER-DG in SeisSol

SeisSol implements the ADER-DG method for elastic (Dumbser & Käser, 2006), viscoelastic (Dumbser et al., 2007b; Uphoff & Bader, 2016), anisotropic (de la Puente et al., 2007; Wolf et al., 2020b) and poroelastic (de la Puente et al., 2008; Wolf et al., 2022) materials. In addition, it supports the coupling of acoustic and elastic domains (Krenz et al., 2023) along with a gravity boundary condition to model tsunami waves (Krenz et al., 2021). SeisSol uses a hybrid parallelization approach using Message Passing Interface (MPI) for multi-node parallelization, and OpenMP. These features allow for the computationally efficient exploration of space-time phenomena in complex wave propagation problems.

SeisSol solves the elastic wave equations written in first-order form as a linear hyperbolic PDE system, as given in eq. (1)

$$\frac{\partial \mathbf{q}}{\partial t} + \mathbf{A}\frac{\partial \mathbf{q}}{\partial x} + \mathbf{B}\frac{\partial \mathbf{q}}{\partial y} + \mathbf{C}\frac{\partial \mathbf{q}}{\partial z} = \mathbf{S}. \tag{28}$$

An additional source term is indicated by $\mathbf{S}$. The PDE system is solved using a high-order Discontinuous Galerkin (DG) method, which discretises the domain into unstructured tetrahedral elements. In each element, the numerical solution is represented by space-dependent, orthogonal polynomial basis functions. The Arbitrary high-order DERivatives (ADER) method (Titarev & Toro, 2002; Dumbser et al., 2008) is used for time integration. The resulting ADER-DG scheme combines a high-order element-local predictor with a corrector step that considers how the local solution depends on neighbor elements by solving Riemann problems. We refer to Dumbser & Käser (2006) and Dumbser et al. (2007b) for details of the ADER-DG method, and to Uphoff et al. (2017) and Uphoff & Bader (2020) for details of the ADER-DG implementation in SeisSol.

In each element k, the numerical solution for the nth timestep is stored as a matrix $\mathbf{Q}_k^n$ of polynomial coefficients, with

the quantities and polynomial basis functions as row and column dimensions of the matrix. The DG discretization in space turns eq. (28) into this equation for each element of the grid

$$\mathbf{D}^1 = \mathbf{M}^{-1}\left(\left(\mathbf{K}^{\xi}\right)^T\mathbf{Q}^n\mathbf{A}^* + \left(\mathbf{K}^{\eta}\right)^T\mathbf{Q}^n\mathbf{B}^* + \left(\mathbf{K}^{\zeta}\right)^T\mathbf{Q}^n\mathbf{C}^*\right), \tag{29}$$

where the mass matrix $\mathbf{M}$ and the stiffness matrices $\mathbf{K}^{\xi}$, $\mathbf{K}^{\eta}$, and $\mathbf{K}^{\zeta}$ result from the choice of the element-local basis functions. As we use orthogonal basis functions, $\mathbf{M}$ becomes diagonal. The matrices $\mathbf{A}^*$, $\mathbf{B}^*$, and $\mathbf{C}^*$ are linear combinations of the matrices $\mathbf{A}$, $\mathbf{B}$, and $\mathbf{C}$ from eq. (28), depending on the orientation of the element.

The first step in the ADER-DG scheme is a Taylor series expansion of the element-local space-time solution $\mathbf{I}$, for which we iterate over eq. (29) to compute the δth derivatives $\mathbf{D}^{\delta}$ for $0 \leq \delta \leq O$, with O the discretization order

$$\mathbf{D}^0 := \mathbf{Q}, \quad \mathbf{D}^{\delta+1} := \mathbf{M}^{-1}\left(\left(\mathbf{K}^{\xi}\right)^T\mathbf{D}^{\delta}\mathbf{A}^* + \left(\mathbf{K}^{\eta}\right)^T\mathbf{D}^{\delta}\mathbf{B}^* + \left(\mathbf{K}^{\zeta}\right)^T\mathbf{D}^{\delta}\mathbf{C}^*\right) \tag{30}$$

and then compute the space-time predictor as

$$\mathbf{I} = \sum_{\delta=0}^{O}\frac{\Delta t^{\delta+1}}{(\delta+1)!}\mathbf{D}^{\delta}, \tag{31}$$

which is referred to as the so-called Cauchy-Kovalevskaya procedure (Dumbser & Käser, 2006). From these space-time predictions $\mathbf{I}$, an explicit update scheme for a time step can be derived

$$\mathbf{Q}^{n+1,*} = \mathbf{Q}^n + \mathbf{I}_{\text{vol}}\left(\mathbf{I}\right) - \mathbf{I}^{\text{local}}_{\text{surf}}\left(\mathbf{I}\right) - \mathbf{I}^{\text{surf}}_{\text{neigh}}\left(\mathbf{I}_{(i)}\right) + \mathbf{I}_{\text{src}}, \tag{32}$$

where the terms $\mathbf{I}_{\text{vol}}$ correspond to the volume discretization, the terms $\mathbf{I}^{\text{local}}_{\text{surf}}$ and $\mathbf{I}^{\text{global}}_{\text{surf}}$ to the numerical fluxes on the element surfaces, and $\mathbf{I}_{\text{src}}$ to the discretization of source terms. The volume term is computed as

$$\mathbf{I}_{\text{vol}}\left(\mathbf{I}\right) = \mathbf{M}^{-1}\left(\mathbf{K}^{\xi}\mathbf{I}\mathbf{A}^* + \mathbf{K}^{\eta}\mathbf{I}\mathbf{B}^* + \mathbf{K}^{\zeta}\mathbf{I}\mathbf{C}^*\right), \tag{33}$$

with all terms known from eq. (29). The surface contributions $\mathbf{I}^{\text{local}}_{\text{surf}}$ and $\mathbf{I}^{\text{neigh}}_{\text{surf}}$ are computed from contributions from all four faces of the tetrahedral cell

$$\begin{aligned}
\mathbf{I}^{\text{local}}_{\text{surf}}\left(\mathbf{I}\right) &= \frac{1}{|J|}\mathbf{M}^{-1}\left(\sum_{i=1}^{4}|S_i|\,\mathbf{F}^{-,i}\mathbf{I}\hat{\mathbf{A}}^{+}\right), \\
\mathbf{I}^{\text{neigh}}_{\text{surf}}\left(\mathbf{I}_{(i)}\right) &= \frac{1}{|J|}\mathbf{M}^{-1}\left(\sum_{i=1}^{4}|S_i|\,\mathbf{F}^{+,i,j,h}\mathbf{I}_{(\mathbf{i})}\hat{\mathbf{A}}^{-}_{(i)}\right),
\end{aligned} \tag{34}$$

where $|J|$ is the volume of the element and $|S_i|$ is the surface area of the ith face. The flux matrices $\mathbf{F}^{-,i}$ and $\mathbf{F}^{+,i,j_k,h_k}$ for each element k and for each face i depend on the choice of the basis functions and the relative position of the element with the respective neighbor (Dumbser & Käser, 2006).$\hat{\mathbf{A}}^{+}_{k}$, $\hat{\mathbf{A}}^{-}_{k(i)}$ are defined as $\hat{\mathbf{A}}^{+}_{k} = \frac{1}{2}\left(\hat{\mathbf{A}}_k + \left|\hat{\mathbf{A}}_k\right|\right)$, and $\hat{\mathbf{A}}^{-}_{k(i)} = \frac{1}{2}\left(\hat{\mathbf{A}}_{k(i)} - \left|\hat{\mathbf{A}}_{k(i)}\right|\right)$, where the notation of the absolute value of the Jacobian matrix has the meaning of applying the absolute value operator to the given eigenvalues (Dumbser & Käser, 2006, eq. 15 in).

We can write the source term $\mathbf{I}_{\text{src}}$ associated with a single point source

$$\mathbf{I}_{\text{src}} = |J|\left(\sum_{j=1}^{O}\omega_j s_{\text{ps}}\left(\tau_j\right)\right)\Psi\left(\xi_s\right), \tag{35}$$

where ω_j are integration weights, s_{ps} is the time-dependent component of the source term inside a mesh element, Ψ_k are space-dependent basis functions on the reference element, and ξ_s is the location of the point source in the reference coordinate system. In this work we consider only point source simulations, but our SeisSol ITM can be generally applied to wavefields excited by extended finite sources. As none of the components required for the calculation of $\mathbf{I}_{\text{src}}$ depend on material properties, these do not need to be revised for the ITM implementation.

3.2 ITM wavefield manipulations in SeisSol

We implement an ITM for elastic waves by modifying the material properties to $\hat{\lambda}$, $\hat{\mu}$, and $\hat{\rho}$ for $t^{-}_{\text{ITM}} \leq t \leq t^{+}_{\text{ITM}}$. Elastic body waves propagate as a P wave or S wave, hence it is possible to reverse both waves together by changing the impedance or just one of the wave types without affecting the other. Here we analyze P wave and S wave scenarios, which significantly extends previous work on ITM effects on elastic waves (Innanen, 2018; Wapenaar et al., 2024). To change the impedance contrast we

can modify the density and keep the Lamé parameters constant or scale them in different proportions. In the following Eqs (36) to (38), n denotes the impedance scaling factor.

3.2.1 Manipulating P waves and S waves

To reflect both waves, we modify the material parameters for the duration of the ITM from t^-_{ITM} to t^+_{ITM} as

$$\begin{aligned} \hat{\lambda} &= n^2\lambda, \\ \hat{\mu} &= n^2\mu, \\ \hat{\rho} &= \rho. \end{aligned} \tag{36}$$

3.2.2 Manipulating P waves only

To reflect only P waves, we modify the material parameters such that only the P wave impedance changes without affecting the S wave impedance. We change the Lamé parameter λ and keep μ constant:

$$\begin{aligned} \hat{\lambda} &= n^2\lambda, \\ \hat{\mu} &= \mu, \\ \hat{\rho} &= \rho. \end{aligned} \tag{37}$$

3.2.3 Manipulating S waves only

Correspondingly, to reflect only S waves, we modify the material parameters such that only the S wave impedance is changed without affecting the impedance of P waves. This is achieved by changing the density and the Lamé parameters:

$$\begin{aligned} \hat{\lambda} &= \frac{\lambda + 2\mu}{n} - 2n\mu, \\ \hat{\mu} &= n\mu, \\ \hat{\rho} &= n\rho. \end{aligned} \tag{38}$$

3.2.4 ITM implementation

The ADER-DG update scheme, as summarized in section 3.1, is formulated as a sequence of element-local matrix operations. As all matrices – with the exception of the quantities $\mathbf{Q}$ – normally remain constant throughout a simulation, SeisSol precomputes and stores all involved matrices during its setup phase. While $\mathbf{K}^{\xi}$, $\mathbf{K}^{\eta}$, $\mathbf{K}^{\zeta}$, and $\mathbf{M}$, as well as the flux matrices $\mathbf{F}^{-,i}$ and $\mathbf{F}^{+,i,j_k,h_k}$ depend on the discretization and on the geometry of the mesh elements, the matrices $\mathbf{A}^*$, $\mathbf{B}^*$, $\mathbf{C}^*$ depend directly on $\mathbf{A}$, $\mathbf{B}$, $\mathbf{C}$, which are again sensitive to the material parameters. Similarly, $\hat{\mathbf{A}}^+$ and $\hat{\mathbf{A}}^-_{(i)}$ contribute to the Riemann solution, which also depends on the local material parameters. Therefore, when the medium parameters change at a time interface, we recompute all matrices $\mathbf{A}^*$, $\mathbf{B}^*$ and $\mathbf{C}^*$, as well as $\hat{\mathbf{A}}^+$ and $\hat{\mathbf{A}}^-_{(i)}$, for all DG elements.

As an explicit scheme, ADER time stepping must obey a Courant–Friedrichs–Lewy (CFL) condition (Lewy et al., 1928). For the elastic wave equation, the allowed time step size is inversely proportional to the largest wave speed c_p. SeisSol employs clustered local time stepping (LTS) (Dumbser & Käser, 2006; Breuer et al., 2016), which groups elements with similar time step sizes into clusters and enforces the CFL condition per LTS cluster. Temporally changing material parameters for ITM requires that we also update the time step sizes, to match the changed wave speeds. Since ITM scaling keeps the ratios between time step sizes of elements and clusters identical, LTS clusters can stay unchanged, and only the time steps for each LTS cluster need to be updated. ITM is thus compatible with utilizing LTS.

3.3 Numerical convergence test

We perform numerical convergence analysis to verify our implementation. We compare SeisSol synthetics of instantaneous time-mirrored acoustic waves to the analytical solution of a propagating planar acoustic wave discussed in Section 2.2. To

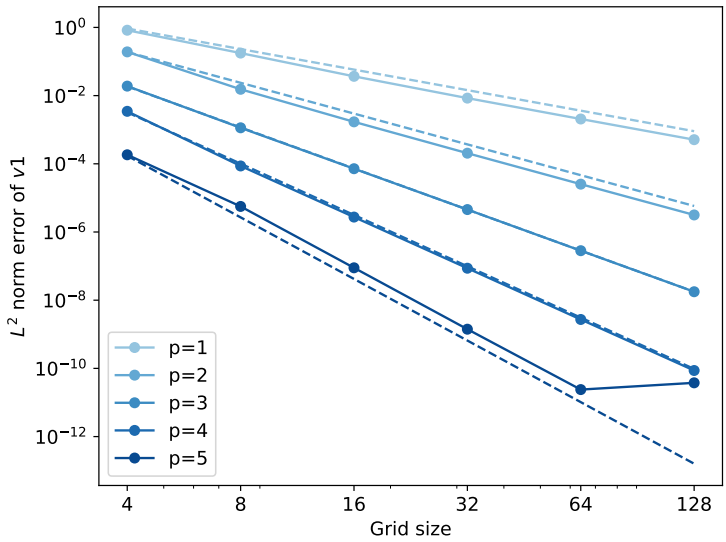

Figure 3. Convergence of the numerical SeisSol response to an instantaneous time mirror and the corresponding analytical plane wave solution for an acoustic medium (eq. 17). The grid size dependent L^2 norm of the differences in the v_1 velocity shows a positive dependence on the polynomial order p. The dashed lines show the theoretical convergence of $p + 1$ for polynomial order p.

quantify convergence, we compute the L^2 norm of the error of the v_1 velocity component of our numerical solution in response to a sinusoidal plane wave excitation with eq. (22) in Section 2.2. For this experiment we use $\tau = 0.01$ s and $n = 2$. We use a series of meshes consisting of uniformly-sized tetrahedral elements in an 8 m^3 cubic domain. We increase the number of elements in each direction as $4, 8, 16, 32, 64, 128$ and examine the error for polynomial orders $p \in \{1, 2, 3, 4, 5\}$. We expect a convergence order of $p+1$ for a polynomial order p used in the DG scheme (Käser & Dumbser, 2006). The results are summarized in the decimal log-log plot in Fig. 3. The slope of the obtained relationships increases as expected with the polynomial order. For order $p = 5$, we observe an increase in error for the smallest grid size with 128 elements, which is due to reaching the limit of floating-point accuracy. We perform a linear fit of the error decimal logarithm and the grid size decimal logarithm to estimate the approximate convergence order obtained with our implementation. From the results in Table 1 we can conclude that our numerical discretization of the ITM converges with the expected order.

Table 1. Convergence order vs polynomial order obtained from the convergence study of acoustic traveling wave with ITM.

Polynomial Order	1	2	3	4	5
Convergence Order	2.13	3.15	4.00	5.03	5.77

4 RESULTS FROM POINT SOURCE SIMULATIONS

We simulate the response of propagating wavefields that are excited by an impulse point source to time boundaries, first for an acoustic medium (Section 4.1) and then for an elastic case (Section 4.2). We use the half-space material parameters of the SISMOWINE WP2_LOH1 code validation benchmark (Moczo et al., 2006) that has been used to evaluate and compare the accuracy and performance of different wave propagation solvers. This benchmark scenario provides a reference for validating free-surface and internal interface wavefield responses. For the acoustic material we set $\mu = 0$ and adapt λ to yield the same P wave speed as in the elastic case. We apply a standard seismic source time function at the center of the domain. The source time function $\dot{S}$ is a Brune source time function (Fig. 4) that approximates an impulse force

$$\dot{S} = \frac{1}{T^2} t e^{-\frac{t}{T}}, \tag{39}$$

where t denotes time and T controls the width of the pulse approximating the duration of the source. This function is scaled by a seismic moment tensor that parameterizes a pressure source and a double couple source, or by a point force applied in the vertical direction. We use a conservatively large computational domain to avoid spurious reflections from non-perfectly absorbing boundaries. All 2D wavefield images (Figs 5 to 10) are generated using the higher-order output feature of SeisSol and are post-processed using the in-house 'light-quake-visualizer' tool.

4.1 The simulated response of an acoustic wavefield to time interfaces

We focus on the acoustic solution in response to a permanent change associated with a single time interface and compare key characteristics to theoretical predictions collected by Wapenaar et al. (2024) to corroborate our results. Then we discuss the refocusing behavior associated with an ITM and connect the results to observations from established time reversal applications. We first apply time interfaces to a P wave generated by a pressure impulse point source in an acoustic material. The initial material properties are

$$\begin{aligned} \rho &= 2700\,\frac{\mathrm{kg}}{\mathrm{m}^3}, \\ \mu &= 0\,\mathrm{Pa}, \\ \lambda &= 9.72 \cdot 10^{10}\,\mathrm{Pa}, \end{aligned} \tag{40}$$

which lead to a P wave speed of $c_p = 6000$ m/s. The mesh used in this scenario resolves frequencies up to 10 Hz with these material properties (Käser et al., 2008). In the scenario where there is only one time interface, we resolve a higher frequency

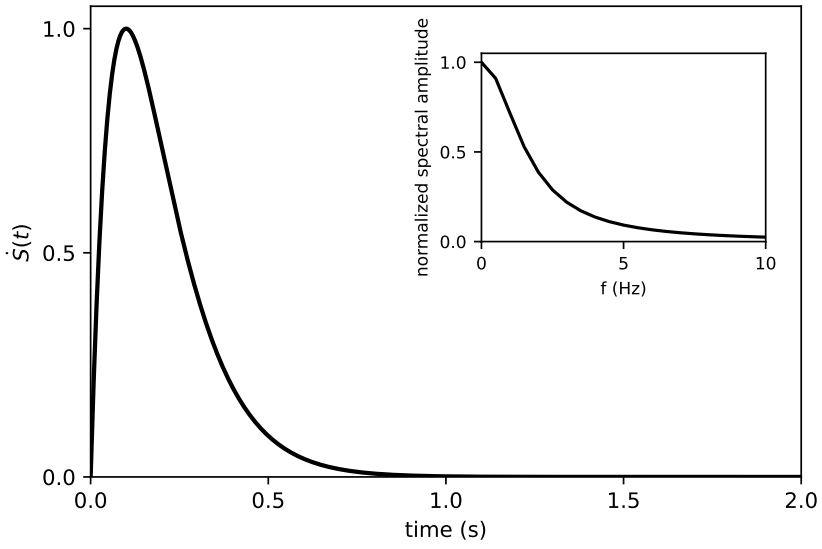

Figure 4. The source time function (eq. 39) used for the velocity impulse point source. The inset shows the normalized spectral amplitude of the source time function.

range due to the modified material parameters. The time interface parameters are

$$\begin{aligned} \tau &= 0.001\,\mathrm{s}, \\ n &= 10, \\ t^{-}_{\mathrm{ITM}} &= 5.0\,\mathrm{s}, \end{aligned} \tag{41}$$

where τ is the duration of the ITM, and n is the impedance scaling factor from eq. (36). These parameters result in the clean responses shown in Figs 1(b) and (c), 5, and 6 obtained with the SeisSol time interface implementation.

4.1.1 Reflection and transmission coefficients and frequency shift at a single time boundary

We first neglect phase III and the associated τ parameter in eq. (41) to compare features of our simulated single time interface responses to theoretical results. For a 1D space boundary it is well known that the wavenumber of a planar wave changes according to $k_{\mathrm{II}} = k_{\mathrm{I}} c_{\mathrm{I}}/c_{\mathrm{II}}$ and the frequency is invariant, $\omega_{\mathrm{II}} = \omega_{\mathrm{I}}$. Correspondingly, for a time boundary, the wavenumber is invariant, $k_{\mathrm{II}} = k_{\mathrm{I}}$, but the frequency changes, $\omega_{\mathrm{II}} = \omega_{\mathrm{I}} c_{\mathrm{I}}/c_{\mathrm{II}}$ (Wapenaar et al., 2024). This means that for our time impedance factor $n = 10$, which yields a ten-fold increase in the pressure wave speed, the frequencies of the reflected and transmitted waves are also expected to increase significantly. Similar to the established 1D planar wave reflection and transmission coefficients R_x and T_x for a space boundary, Wapenaar et al. (2024) developed R_t and T_t expressions for a time boundary

$$\begin{aligned} R_t &= \frac{1}{2}\left(\frac{\lambda_{\mathrm{I}}}{\lambda_{\mathrm{II}}} - \frac{c_{\mathrm{II}}}{c_{\mathrm{I}}}\right), \\ T_t &= \frac{1}{2}\left(\frac{\lambda_{\mathrm{I}}}{\lambda_{\mathrm{II}}} + \frac{c_{\mathrm{II}}}{c_{\mathrm{I}}}\right), \end{aligned} \tag{42}$$

where λ is the bulk modulus, $c = c_p$, and the subscripts I and II refer again to the two phases before and after the time boundary, respectively, equivalent to the λ and $\hat{\lambda}$ notation in Section 3.2. This behavior is illustrated in Fig. 1(b), where we can observe the incident 6 km/s wave speed up to $t < 5$ s (eq. 41), and then a ten-fold increase in the reflected and transmitted wave speeds for $t > 5$ s.

To analyze the frequency content we compute the Fourier amplitude spectra of 2 s long zero-padded waveforms of the incident, reflected, and transmitted waves. The spectrum of the comparatively broad incident waveform (Fig. 1b) shows energy in the $0{-}10$ Hz range and a peak around $1.5{-}2$ Hz. The spectra associated with the significantly more narrow reflected and transmitted wavelets is correspondingly broader, with an observed peak around 15 Hz. This shift in the peak energy is thus in good agreement with the predicted shift of the central frequency by a factor of $\omega_{\mathrm{II}}/\omega_{\mathrm{I}} \approx c_{\mathrm{II}}/c_{\mathrm{I}} = 10$.

The theoretical reflection and transmission coefficients (eq. 42) for our material values (eq. 40) and $n = 10$ are $R_t = -4.995$ and $T_t = 5.005$, respectively. When we scale these values by the simulated incident amplitude of about -0.4, neglecting the order of magnitude of the considered normal stress values, we obtain estimates around $+2.0$ and -2.0, which are in good agreement with the simulated reflected and transmitted amplitudes of $+1.9$ and -1.8, respectively. These values are obtained for the broadband signals but also for narrowband filtered waveforms using a Gaussian filter with 1.5 Hz and 15 Hz central frequency. The shift to higher frequencies and the R_t and T_t coefficient results demonstrate that our SeisSol simulations of the response to a single time boundary are consistent with analytical results of a plane wave model. We attribute the residuals to the differences between the model assumptions and the 3D numerical solution.

4.1.2 Acoustic ITM refocusing and focal spot properties

The next step is the application of a second time boundary (Fig. 1c) after τ s that completes a time slab or the ITM. We use a first example to demonstrate again the SeisSol effectiveness by connecting the properties of the simulated refocusing pattern or focal spot to results in the literature. The acoustic medium properties and time boundary values (eqs 40, 41) result in the 10 s long clean response obtained with the SeisSol ITM implementation illustrated in Fig. 5, where the visualization plane intersects the source location, and the indicated times are relative to t^{-}_{ITM}. The top five panels show the diverging P^{+} wave that interacts with the ITM at $t = 0$ s. The $t = 0.3$ s panel shows the P^{+} wave together with the new converging P^{-} wave that

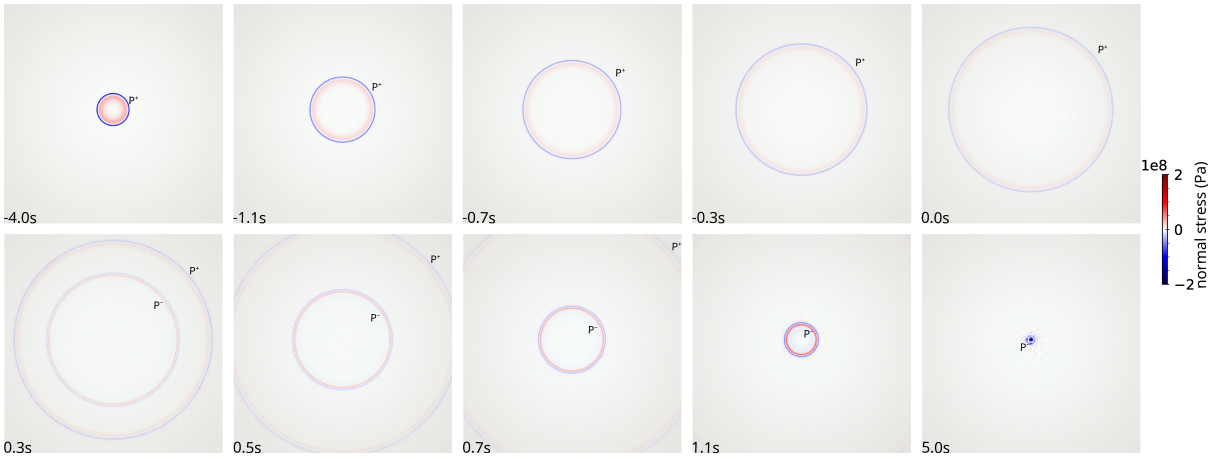

Figure 5. The response of an acoustic wavefield to an instantaneous time mirror activated at $t = 0.0$ s. The labels P^+ and P^- indicate the diverging and converging wave, respectively. The panels show a 2D section of the spherical wavefield in the y-z plane through the location of the pressure impulse moment tensor point source. The colorrange is clipped.

refocuses at $t = 5$ s. Note that the red-blue amplitude pattern of the P^+ and P^- waves illustrates the first in-last out symmetry associated with the ITM response (Bacot et al., 2016).

The spatiotemporal pressure field σ_{xx} is shown in an alternative illustration in Fig. 6(b). In the left part of the main panel it shows the converging wave that has been reflected by the ITM at $t = 5$ s before it refocuses at $t = 10$ s around the source position at 3 km and then diverges again in the right part. The slopes indicate the 6 km/s propagation speed. The corresponding cross sections show the normal stress amplitude distributions along $x = 3$ km (Fig. 6a) and at $t = 10$ s (Fig. 6c). The large amplitude feature around the origin at the refocusing time is referred to as focal spot. The finite width of the focal spot is a consequence of the interacting converging and diverging parts of the wavefield. For seismic surface waves the focal spot is the time domain equivalent of the well known spatial autocorrelation (Aki, 1957; Hillers et al., 2016; Giammarinaro et al., 2022; Tsarsitalidou et al., 2024). For a monochromatic body wave the focal spot shape is described by a sinc function, and its half-width or tip-curvature are a proxy for the local wavelength, and these relationships have been extensively utilized in acoustics and medical imaging applications (Fink, 1997, 2006; Catheline et al., 2008; Gallot et al., 2011). The half-width is the width of the spot measured at half the peak amplitude, and it is an estimate of half a wavelength. In Fig. 6, the indicated half-width at the refocusing time $t = 10$ s is approximately 625 m. The $\sim$5 Hz central frequency of the wave after refocusing and the 6 km/s local wave speed yield a wavelength of 1200 m, which agrees with our half-wavelength estimate. These results from the acoustic case relate our ITM response analysis to established time reversal observations and corroborate the effectiveness and accuracy of our SeisSol simulations.

4.2 The simulated ITM response in an elastic medium

We extend the discussion from an acoustic to an elastic ITM response. We illustrate the general behavior of 3D elastic waves and discuss the three different possibilities of manipulating P waves and S waves, i.e., we mirror the full body wavefield, and the P wave and the S wave separately. We first discuss the evanescent near-field component of the point source solution for moment tensor sources in elastic media. The non-propagating near-field term results from a moment tensor rate with a non-zero integral over the source duration (Secs. 4.2.3 and 2.6.2 in Aki & Richards, 2002; Igel, 2016). An example of this static near-field component is illustrated in the center of the panels in Fig. 7 that show again the σ_{xx} component. The near-field lobes as well as the amplitude distribution of the propagating P wave and S wave are controlled by the radiation pattern of the shear dislocation point source. As in Fig. 5 the visualization plane in Fig. 7 intersects the source location. Hence we can not reconstruct clean focal spots at the source location from the mirrored, converging wavefield as in Fig. 6. Instead, Figs 8 to 10 show the v_3 component of the simulated wavefields in the y-z plane at $x = 2$ km, which better illustrates the ITM response away from the source location at the origin and hence away from the large amplitudes in the near-field.

We apply an ITM to waves excited by point sources. We use the halfspace material parameters of the LOH1 benchmark

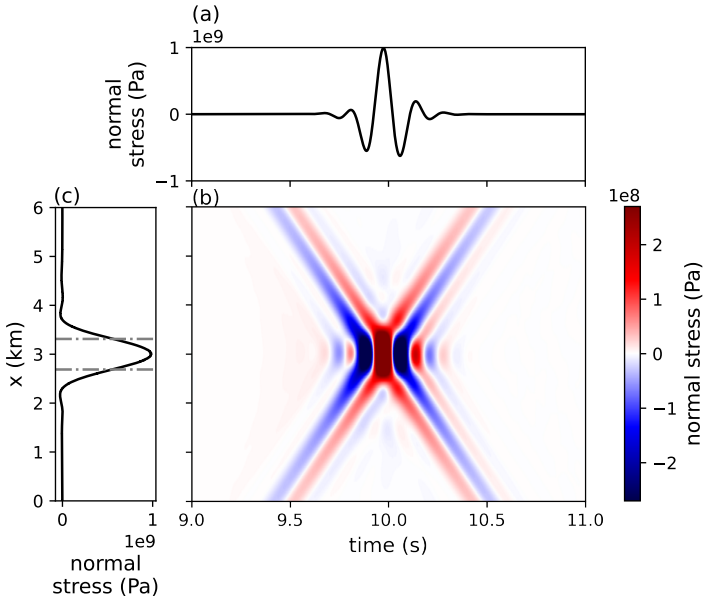

Figure 6. (a) Space-time representation of the time-reversal collapse on the source location for an acoustic pressure wavefield excited by a pressure impulse moment tensor in response to an instantaneous time mirror activated at $t = 5$ s. The spatial and temporal refocusing occurs at $x = 3$ km and $t = 10$ s. The colorrange is clipped. (b) Cross section through the wavefield in panel (a) along the time axis at the location $x = 3$ km. (c) Cross section through the wavefield in panel (a) along the space axis at the refocusing time $t = 10$ s.

scenario

$$\begin{aligned} \rho &= 2700\,\frac{\mathrm{kg}}{\mathrm{m}^3}, \\ \mu &= 3.24 \cdot 10^{10}\,\mathrm{Pa}, \\ \lambda &= 3.24 \cdot 10^{10}\,\mathrm{Pa}, \end{aligned} \tag{43}$$

which lead to P wave and S wave speeds of

$$\begin{aligned} c_p &= 6000\,\frac{\mathrm{m}}{\mathrm{s}}, \\ c_s &= 3464\,\frac{\mathrm{m}}{\mathrm{s}}, \end{aligned} \tag{44}$$

respectively. With these material parameters, the meshes we used can resolve up to 5 Hz in the domain of interest. The ITM parameters are

$$\begin{aligned} \tau &= 0.01\,\mathrm{s}, \\ n &= 10, \\ t_{\mathrm{ITM}}^{-} &= 9\,\mathrm{s}. \end{aligned} \tag{45}$$

for the cases where we reflect both P- and S- waves, for reflection of just the S-wave, we use a scaling factor of $n = 0.1$. To manipulate the wavefield for the three cases,, the value of the impedance scaling factor n is applied in the corresponding eqs (36), (37), or (38). As before, these parameters yield the clean responses exhibited in Figs 8 to 10.

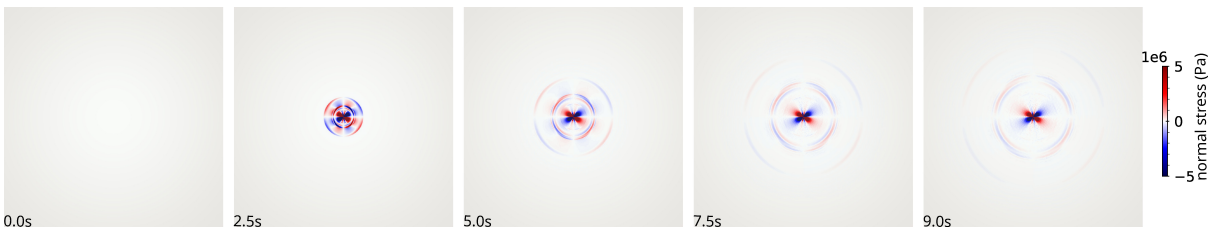

Figure 7. Illustration of an elastic wavefield in response to a moment tensor point source. The amplitudes of the propagating P waves and S waves decay away from the seismic moment tensor source, in contrast to the comparatively large-amplitude static near-field component. The colorrange is clipped.

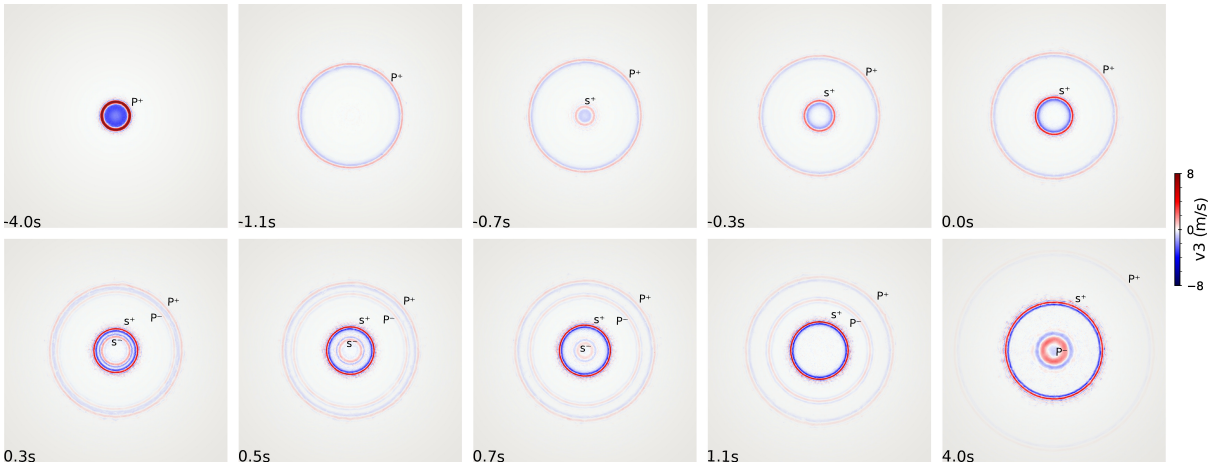

Figure 8. The response of an elastic wavefield to an instantaneous time mirror activated at $t = 0.0$ s. The intermittent change in the elastic parameters affects the P wave and the S wave. The superscripts $+$ and $-$ indicate the diverging and converging components, respectively. The panels show a 2D section of the spherical wavefield in the x-y plane at $z = 28$ km in response to a vertical velocity impulse point force located at the origin. The colorrange is clipped.

The panels in the top row in Fig. 8 show the diverging P^+ and S^+ waves in the visualization plane around $t = -4$ s and $t = -0.7$ s, respectively. At $t = 0.3$ s we can again discern the first in-last out symmetry of the amplitude pattern of the converging P^- and S^- waves that are created by the ITM at $t = 0$ s. All four waves continue to propagate, and around $t = 0.7$ s and $t = 4$ s the S^- wave and the P^- wave are about to 'exit' the visualization plane, respectively.

Fig. 9 exhibits the same features at the same times, except that only a converging P^- wave emerges at $t = 0.3$ s in response to the ITM that leaves the S wave propagation unaffected.

The wavefields in the top row panels in Fig. 10 are again identical to the solutions in Figs 8 and 9, but now only the S^- wave is jolted into existence and propagates back toward the center, where it would refocus and diverge again.

The S wave manipulation is alternatively illustrated in the two representations of the wavefield in Fig. 11. Results in Fig. 11(a) show the space-time pattern along the x–axis at $y = 12$ km, $z = 40$ km, analogous to Fig. 3(a) in Bacot et al. (2016). The profile extends radially away from the source at $(12, 12, 68)$ km. The P wave propagates undisturbed but the converging S^- wave splits away from the diverging S^+ wave at the ITM activation. This highlights again the first in-last out symmetry, e.g., at $t = 0.2$ s. The pattern also exhibits the ITM induced amplitude change of the transmitted S^+ wave, and the change in frequency content. The results in Fig. 11(b) show results from the same simulation in an alternative time-space configuration, where the 20 km long profile ranges from $(16, 12, 40)$ km to $(36, 12, 40)$ km, i.e., from 4 to 24 km relative to

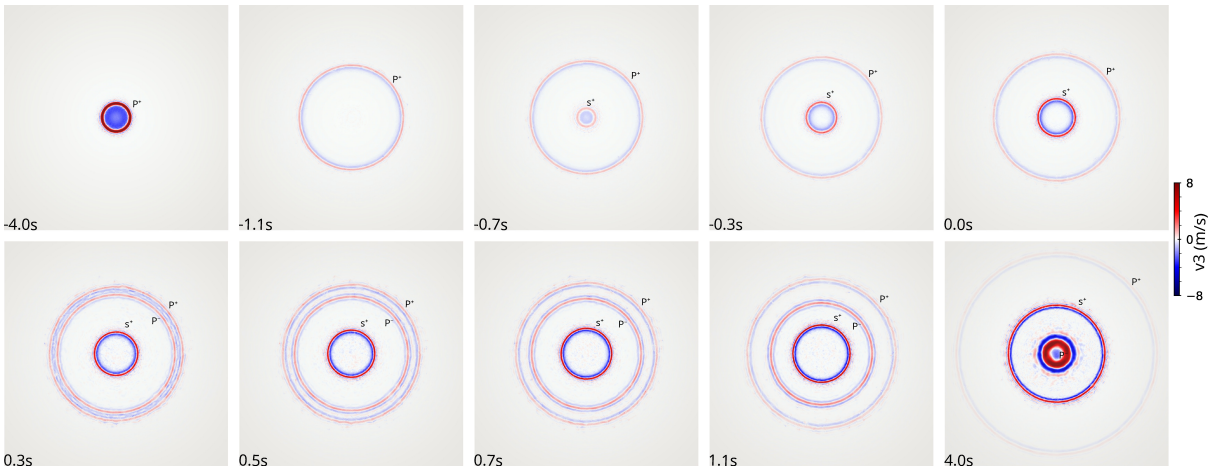

Figure 9. The response of an elastic wavefield to an instantaneous time mirror activated at $t = 0.0$ s. The intermittent change in the elastic parameters affects only the P wave. The superscripts $+$ and $-$ indicate the diverging and converging components, respectively. The panels show a 2D section of the spherical wavefield in the x-y plane at $z = 28$ km in response to a vertical velocity impulse point force located at the origin. The colorrange is clipped.

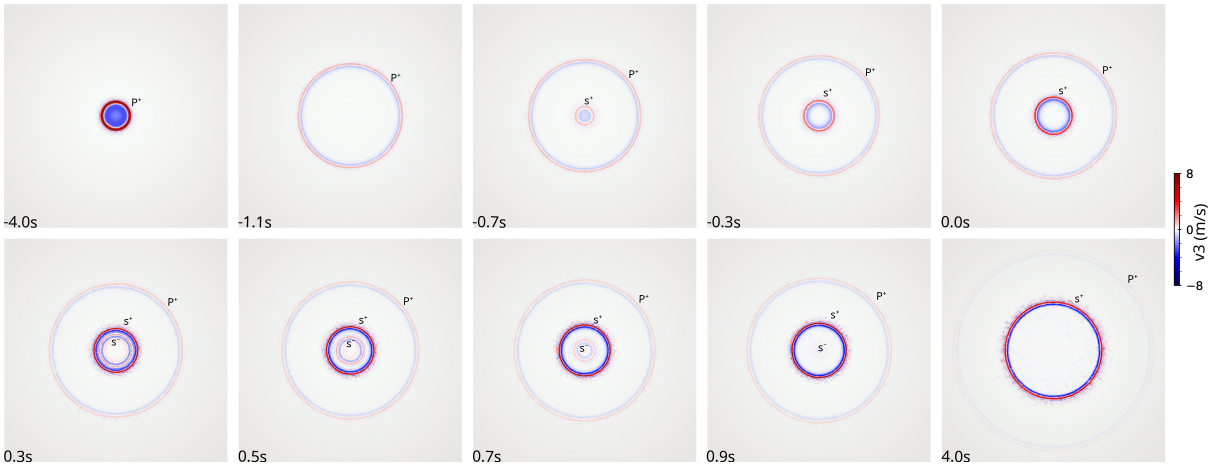

Figure 10. The response of an elastic wavefield to an instantaneous time mirror activated at $t = 0.0$ s. The intermittent change in the elastic parameters affects only the S wave. The superscripts $+$ and $-$ indicate the diverging and converging components, respectively. The panels show a 2D section of the spherical wavefield in the x-y plane at $z = 28$ km in response to a vertical velocity impulse point force located at the origin. The colorrange is clipped.

the source. This profile does not point radially away from the source at $(12, 12, 68)$ km, which explains the different P^+ wave to S^+ wave amplitude ratio for $t < t^-_{\text{ITM}} = 0$ s, the curved wave fronts, and the amplitude decay with distance. The illustration shows the phase change of the ITM affected S waveform, e.g., by comparing the shapes of the S^+ wave and S^- wave at $x = 8$ km. These results together with the images in Figs 8 to 10 highlight the rich and complex space-time features associated with the sampling configuration of 3D elastic wavefields in response to an ITM.

We observe a sensitivity in the simulated phase III amplitudes after t^+_{ITM} (Section 2.2), i.e., the amplitudes of the manipulated waves in the lower row panels in Figs 8 to 10 and in Fig. 11, to our choice of the time impedance scaling factor n. Simulations with n values that are lager than $n = 10$ (eq. 45), or with values that are small compared to unity, lead to significantly larger amplitudes. These observations are compatible with the asymptotic results in eq. (23) illustrated in Fig. 2(b) that show an energy increase with n and $1/n$ in response to the ITM.

All results are obtained with empirically determined τ values in the range between 0.001 s and 0.01 s to provide clean ITM responses for our demonstration purpose. The associated testing results suggest a sensitivity of the amplitude to variations in τ. This cannot, however, be linked to the analytical results in Section 2.2 that exhibit a τ dependence only in the cosine function argument of the reflected and transmitted planar acoustic waves (eq. 22). Updated analytical results for the 3D elastic response to point sources are required for a comprehensive exploration of τ dependent energy scaling.

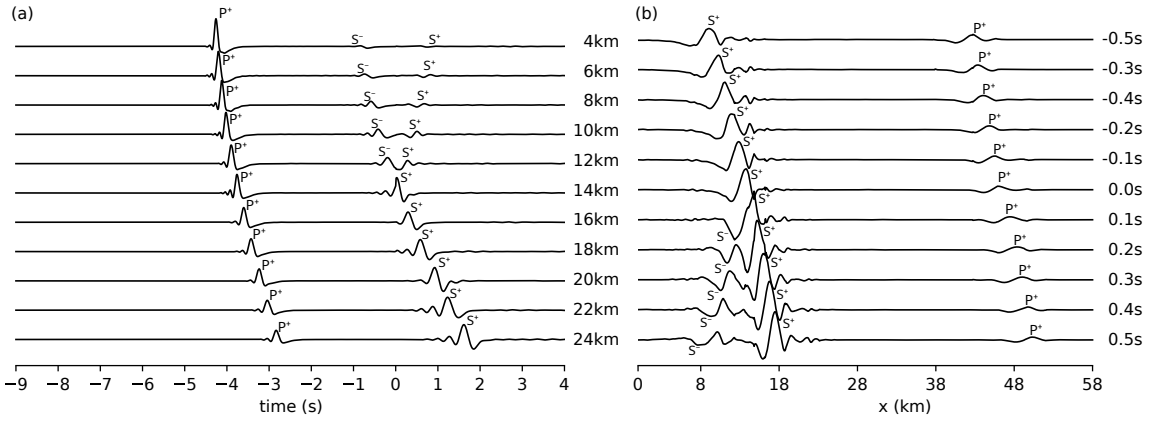

Figure 11. The response of an elastic wavefield to an instantaneous time mirror activated at $t = 0.0$ s using complementary space-time sampling configurations. The intermittent change in the elastic parameters affects only the S wave. (a) The wavefield along a 58 km long profile along the x-axis at $y = 12$ km, $z = 40$ km. The source is located at $(12, 12, 68)$ km. (b) 13 s long seismograms along a 20 km section along the x-axis.

Together our results convincingly illustrate the application of the ITM concept in an elastic medium and show the interesting phenomena to reverse either the full wavefield or any one body wave component independently by intermittently changing the medium parameters. The simulated responses demonstrate the robust implementation of ITM physics in the SeisSol community solver, but also highlight the potential for analytical developments for a more complete ITM energy partitioning theory.

5 DISCUSSION

The space-time analogy in wave propagation (Fig. 1) has led to growing interest in time-dependent manipulation of material properties, where instantaneous changes in elastic properties act as temporal boundaries. Similarities and differences in the responses to space and time dependent changes are governed by the associated changes in boundary and initial conditions, respectively (Bacot et al., 2016; Fink & Fort, 2017; Wapenaar et al., 2024). Our analytical and numerical analyses of the response of a 3D elastic wavefield to a single time interface and to a time slab or instantaneous time mirror (ITM) in a 3D elastic wave propagation framework using the open source code SeisSol advances seismic wavefield manipulations.

We focus on instantaneous changes of the elastic parameters, and thus wave speeds, governed by a scaling factor n at a time interface, in contrast to periodic or other transient temporal variations (Wapenaar et al., 2024). An ITM of duration τ is constructed as a quick succession of two time interfaces, briefly altering and then restoring the original material properties. To validate our simulated 3D responses we establish analytical models that are used to benchmark selected synthetic results and provide insight into the system energy. Using the properties of eigenvalues associated with the matrix structure of a general wave equation (Section 2) and of the 3D elastic wave equation (Section 2.3) we establish a forward and backward propagating plane wave solution in response to a time interface that leads to a permanent medium change.

The plane wave approach is used for an acoustic 1D case (Section 2.2) to build the diverging and converging solutions in response to an ITM, and these solutions yield expressions for the system energy budget that depend on n. It shows that the energy increases for all intermittent medium changes, for all n smaller and larger than unity (Fig. 2), which is compatible with non-steady-state energy considerations based on alternative formulations (Wapenaar et al., 2024) and thus corroborates the observation that a temporal discontinuity changes the energy in the system (Bacot et al., 2016). Importantly, the solutions for the forward and backward propagating plane waves provide the reference for benchmarking the ITM responses.

We implement the time boundaries in the open source software SeisSol. It employs an ADER-DG scheme on unstructured tetrahedral meshes that supports the simulation of dynamic rupture and seismic, acoustic and gravity wave propagation for complex geometries and heterogeneous material properties encountered in Earth Science applications (e.g., Taufiqurrahman et al., 2023; Krenz et al., 2023; Palgunadi et al., 2024). The utilization of the open source code is supported by frequent training events and extensive tutorials (Denolle et al., 2025), which can now also include ITM applications. We use the analytical solutions of the 1D acoustic plane wave propagation to demonstrate the good convergence properties of our numerical implementation (Fig. 3). For this demonstration we force a sinusoidal propagating plane wave. The convergence test establishes the positive dependence of the L^2 norm on the spatial discretization and on the polynomial order. We emphasize that the L^2 norm measures the agreement of both diverging and converging wave components in response to the ITM activation. This corroborates the numerical ITM implementation for the manipulation of a 3D elastic wavefield excited by a point source, for which we do not derive a corresponding reference solution. These results also imply the accuracy of ITM manipulated wavefields excited by finite sources.

A first key result from our 3D acoustic point source simulations involves refocusing in response to an ITM. The collapsing acoustic wavefield yields a large-amplitude feature at the source location (Fig. 6). The properties of this focal spot are controlled by the local medium properties, which supports a wide range of imaging approaches that are complementary to tomographic inversions (Catheline et al., 2008; Gallot et al., 2011; Catheline et al., 2013; Giammarinaro et al., 2022; Tsarsitalidou et al., 2024). Here the good agreement between our P wave speed estimates of $c_P = 6.25$ km/s based on the narrow-band filtered focal spot width (Fig. 6) and the controlled velocity $c_P = 6.00$ km/s supports again the notion of an accurate wave physics implementation in SeisSol. The validity of the implementation is further supported by our estimates of the reflected and transmitted wave amplitudes across a single time interface that are in good agreement with the plane wave predictions by Wapenaar

et al. (2024). This exercise also corroborates the scaling of the frequency content of the reflected and transmitted signals with the impedance scaling factor n, which differs fundamentally from the constant frequency content across an interface in space. In agreement with the water tank results by Bacot et al. (2016) the 2D slices of the ITM manipulated wavefield (Fig. 5) illustrate the first in-last out symmetry of the amplitude pattern that differs from the first in-first out reflections at a space interface and at a time reversal mirror. For the elastic case the large-amplitude static near-field component (Fig. 7) prohibits the width measurements of P wave and S wave focal spots. This is inconvenient for numerical focal spot imaging studies (Giammarinaro et al., 2022, 2024), but it can be mitigated using appropriate filters. Another key result of our implementation is the independent manipulation of P waves and S waves by a selective ITM variation of the impedances (Figs. 9, 10). The intriguing possibility of separating converging P waves from S waves highlights the greater diversity of elastic wavefield phenomena compared to ITM responses for electromagnetic or acoustic propagation. This can support the development of efficient numerical strategies for synthetic wavefield manipulations.

Electromagnetic fields are comparatively easy to manipulate by changing the admittance, in contrast to time dependent variations of Earth materials. Seismic wavefields can be engineered using resonator arrays that can lead to effective seismic metamaterials with the potential to reduce seismic hazard (Colombi et al., 2016; Mu et al., 2020). Backward propagation plays an important role in adjoint tomography solutions (Tromp et al., 2005) and to constrain source locations (McMechan, 1982; Rietbrock & Scherbaum, 1994; Gajewski & Tessmer, 2005; Larmat et al., 2006) and earthquake rupture processes (Krüger & Ohrnberger, 2005; Kiser & Ishii, 2017), which are suitable application cases for the SeisSol software. More generally, our ITM implementation extends the SeisSol computational framework to simulate and explore the effects of time varying properties of Earth materials at different scales. SeisSol has demonstrated its utility in challenging Earth Science multi-physics simulations involving rapid, spatially distributed material changes associated with large earthquakes or tsunamis (Krenz et al., 2021), and provides an integrated numerical environment to research wavefields in space- and time-varying media. As demonstrated, properties of the focal spot or the spatial autocorrelation field are indicators of the local wave speed. Numerical focal spot syntheses based on analytical solutions (Catheline et al., 2008), time reversal mirrors (Giammarinaro et al., 2022), or correlations of scattered or diffuse wavefields (Catheline et al., 2013; Giammarinaro et al., 2024) are essential for method development including robustness and sensitivity analyses. The noise correlation and Green's function analogy (Derode et al., 2003) supports seismic dense array-based Rayleigh wave focal spot imaging (Hillers et al., 2016; Tsarsitalidou et al., 2024) that has not been explored systematically for anisotropic media except for initial observations of azimuthally variable surface wave speeds (Hillers et al., 2016). Focal spot synthesis by time reversal mirroring of Rayleigh wave Green's functions in an azimuthally anisotropic medium (Hillers et al., 2023) is challenging because of the correct implementation of the boundary conditions. Together with the implementation of anisotropic elastic parameters in SeisSol (Wolf et al., 2020a; Hillers et al., 2023) the ITM engine can be used to synthesize focal spots in media with direction dependent properties, provided that the refocusing field is separated from the static near-field components.

In this work we focus on body wave propagation in response to an intermittent change in the material properties of an homogeneous elastic full space. Additional physics and configurations leading to richer phenomena have been investigated in other domains and applications. These include ITM in inelastic, heterogeneous, and dissipating materials (Besten et al., 2021; Wu et al., 2022), time reflection and refraction (Mendonça & Shukla, 2002), incidence angle dependence of reflection and transmission (Pendry, 2008) and wave conversions associated with oblique reflections (Innanen, 2018). Future extensions of our work can explore these concepts and applications for seismic wavefields.

6 CONCLUSIONS

We analyze wavefield behavior in time-varying media that are spatially uniform. Our eigenvector-based analytical solutions model acoustic waves at time interfaces. These models provide a framework for energy balance estimates in jolted systems and are used as reference solutions for our numerical convergence tests. These tests illustrate the effectiveness of the employed SeisSol ADER-DG solution for the numerical simulation of wavefield phenomena in media that are heterogeneous in space and time. Our simulated 3D elastic wavefields in response to an instantaneous time mirror showcase the possibility to manipulate

the complete body wavefield but also to tune the propagation of the P wave and S wave components independently, which emphasizes the richness in seismic wave propagation compared to ITM responses for electromagnetic or acoustic waves.

ACKNOWLEDGMENTS

This work is inspired by a presentation by M. Fink at ISTerre, University Grenoble Alpes, in 2016. We thank S. Wolf for initiating the ITM implementation in SeisSol. We thank D. Schneller for implementing the higher-order output used for the wavefield visualizations (funded by KONWIHR, Competence Network for Scientific High Performance Computing in Bavaria). VK, LK, AAG, and MB acknowledge funding provided (as part of the EuroHPC Joint Undertaking) for the ChEESE-2P cluster of excellence by Horizon Europe (grant agreement No. 101093038) and by the German Federal Ministry of Research, Technology and Space. GH acknowledges support from the Research Council of Finland (Flagship of Advanced Mathematics for Sensing Imaging and Modelling grant 359182 and grant 322421). AAG acknowledges additional support from Horizon Europe (DT-GEO, grant number 101058129 and Geo-INQUIRE, grant number 101058518), the National Science Foundation (NSF grant numbers CRESCENT EAR-2225286, MTMOD EAR-2121568, LCCF-CSA OAC-2323116, QUAKEWORX OAC-2311208), the National Aeronautics and Space Administration (NASA 80NSSC20K0495) and the Statewide California Earthquake Center (SCEC projects 25259, 25313, 25341). The CSC IT Center for Science, Finland, grand challenge Project Number 2003841 provided access to the CSC Mahti computational infrastructure.

DATA AVAILABILITY

The simulation files for the point source simulations with acoustic and elastic materials can be found at `https://doi.org/10.5281/zenodo.15877555`. The Sismowine LOH1 benchmark scenario is described in `http://www.sismowine.org/model/WP2_LOH1.pdf`. Details of the implementation of point sources in SeisSol are discussed in `https://seissol.readthedocs.io/en/latest/point-source-older-implementation.html`. Details about installing and running SeisSol can be found at `https://seissol.readthedocs.io/en/latest/build-overview.html`

References

Aki, K., 1957. Space and time spectra of stationary stochastic waves, with special reference to microtremors, *Bull. Earthquake Res. Inst. Univ. Tokyo*, **35**, 415–457.

Aki, K. & Richards, P. G., 2002. *Quantitative Seismology*, University Science Books, 2nd edn.

Bacot, V., Labousse, M., Eddi, A., Fink, M., & Fort, E., 2016. Time reversal and holography with spacetime transformations, *Nature Physics*, **12**(10), 972–977, 10.1038/nphys3810.

Besten, J. G. M., Marks, B., & Einav, I., 2021. Reversing and amplifying elastic waves in inelastic granular media, *Granular Matter*, **24**(1), 10.1007/s10035-021-01180-9.

Breuer, A., Heinecke, A., & Bader, M., 2016. Petascale Local Time Stepping for the ADER-DG Finite Element Method, in *2016 IEEE International Parallel and Distributed Processing Symposium (IPDPS)*, pp. 854–863.

Castanheira-Pinto, A., Alves-Costa, P., Godinho, L., & Amado-Mendes, P., 2018. On the application of continuous buried periodic inclusions on the filtering of traffic vibrations: A numerical study, *Soil Dynamics and Earthquake Engineering*, **113**, 391–405, 10.1016/j.soildyn.2018.06.020.

Catheline, S., Benech, N., Brum, J., & Negreira, C., 2008. Time Reversal of Elastic Waves in Soft Solids, *Phys. Rev. Lett.*, **100**, 064301, 10.1103/PhysRevLett.100.064301.

Catheline, S., Souchon, R., Rupin, M., Brum, J., Dinh, A. H., & Chapelon, J.-Y., 2013. Tomography from diffuse waves: Passive shear wave imaging using low frame rate scanners, *Applied Physics Letters*, **103**(1), 014101, 10.1063/1.4812515.

Colombi, A., Colquitt, D., Roux, P., Guenneau, S., & Craster, R. V., 2016. A seismic metamaterial: The resonant metawedge, *Scientific Reports*, **6**(1), 27717, 10.1038/srep27717.

de la Puente, J., Käser, M., Dumbser, M., & Igel, H., 2007. An arbitrary high-order discontinuous Galerkin method for elastic waves on unstructured meshes - IV. Anisotropy, *Geophysical Journal International*, **169**(3), 1210–1228, 10.1111/j.1365-246X.2007.03381.x.

de la Puente, J., Dumbser, M., Käser, M., & Igel, H., 2008. Discontinuous Galerkin methods for wave propagation in poroelastic media, *GEOPHYSICS*, **73**(5), T77–T97, 10.1190/1.2965027.

Denolle, M. A., Tape, C., Bozdağ, E., Wang, Y., Waldhauser, F., Gabriel, A., Braunmiller, J., Chow, B., Ding, L., Feng, K., Ghosh, A., Groebner, N., Gupta, A., Krauss, Z., McPherson, A. M., Nagaso, M., Niu, Z., Ni, Y., Örsvuran, R., Pavlis, G., Rodriguez-Cardozo, F., Sawi, T., Schaff, D., Schliwa, N., Schneller, D., Shi, Q., Thurin, J., Wang, C., Wang, K., Wong, J. W. C., Wolf, S., & Yuan, C., 2025. Training the next generation of seismologists: Delivering research-grade software education for cloud and hpc computing through diverse training modalities, *Seismological Research Letters*, 10.1785/0220240413.

Derode, A., Larose, E., Tanter, M., de Rosny, J., Tourin, A., Campillo, M., & Fink, M., 2003. Recovering the Green's function from field-field correlations in an open scattering medium (L), *The Journal of the Acoustical Society of America*, **113**(6), 2973–2976, 10.1121/1.1570436.

Dijckmans, A., Ekblad, A., Smekal, A., Degrande, G., & Lombaert, G., 2016. Efficacy of a sheet pile wall as a wave barrier for railway induced ground vibration, *Soil Dynamics and Earthquake Engineering*, **84**, 55–69, 10.1016/j.soildyn.2016.02.001.

Dumbser, M. & Käser, M., 2006. An arbitrary high-order discontinuous Galerkin method for elastic waves on unstructured meshes — II. The three-dimensional isotropic case, *Geophysical Journal International*, **167**(1), 319–336, 10.1111/j.1365-246X.2006.03120.x.

Dumbser, M., Käser, M., & Toro, E. F., 2007a. An arbitrary high-order Discontinuous Galerkin method for elastic waves on unstructured meshes - V. Local time stepping and p-adaptivity, *Geophysical Journal International*.

Dumbser, M., Käser, M., & Toro, E. F., 2007b. An arbitrary high-order Discontinuous Galerkin method for elastic waves on unstructured meshes – V. Local time stepping and p-adaptivity, *Geophysical Journal International*, **171**(2), 695–717, 10.1111/j.1365-246X.2007.03427.x.

Dumbser, M., Balsara, D. S., Toro, E. F., & Munz, C.-D., 2008. A unified framework for the construction of one-step finite volume and discontinuous Galerkin schemes on unstructured meshes, *Journal of Computational Physics*, **227**(18), 8209–8253, https://doi.org/10.1016/j.jcp.2008.05.025.

Ekström, G., Abers, G. A., & Webb, S. C., 2009. Determination of surface-wave phase velocities across USArray from noise and Aki's spectral formulation, *Geophysical Research Letters*, **36**(18), 10.1029/2009GL039131.

Evans, L. C., 2010. *Partial Differential Equations: Second Edition*, vol. 19.R of **Graduate Series in Mathematics**.

Fink, M., 1997. Time reversed acoustics, *Physics Today*, **50**(3), 34–40, 10.1063/1.881692.

Fink, M., 2006. Time-reversal acoustics in complex environments, *GEOPHYSICS*, **71**(4), SI151–SI164.

Fink, M. & Fort, E., 2017. From the time-reversal mirror to the instantaneous time mirror, *The European Physical Journal Special Topics*, **226**(7), 1477–1486, 10.1140/epjst/e2016-60258-8.

Gabriel, A.-A., Kurapati, V., Niu, Z., Schliwa, N., Schneller, D., Ulrich, T., Dorozhinskii, R., Krenz, L., Uphoff, C., Wolf, S., Breuer, A., Heinecke, A., Pelties, C., Rettenberger, S., Wollherr, S., & Bader, M., 2025. Seissol.

Gajewski, D. & Tessmer, E., 2005. Reverse modelling for seismic event characterization, *Geophysical Journal International*, **163**(1), 276–284, 10.1111/j.1365-246X.2005.02732.x.

Galiffi, E., Xu, G., Yin, S., Moussa, H., Ra'di, Y., & Alù, A., 2023. Broadband coherent wave control through photonic collisions at time interfaces, *Nature Physics*, **19**(11), 1703–1708, 10.1038/s41567-023-02165-6.

Gallot, T., Catheline, S., Roux, P., Brum, J., Benech, N., & Negreira, C., 2011. Passive elastography: shear-wave tomography from physiological-noise correlation in soft tissues, *IEEE Transactions on Ultrasonics, Ferroelectrics, and Frequency Control*, **58**(6), 1122–1126, 10.1109/TUFFC.2011.1920.

Gérardin, B., Laurent, J., Legrand, F., Prada, C., & Aubry, A., 2019. Negative reflection of elastic guided waves in chaotic and random scattering media, *Scientific Reports*, **9**(1), 2135, 10.1038/s41598-019-38480-3.

Giammarinaro, B., Tsarsitalidou, C., Hillers, G., de Rosny, J., Seydoux, L., Catheline, S., Campillo, M., & Roux, P., 2022. Seismic surface wave focal spot imaging: numerical resolution experiments, *Geophysical Journal International*, **232**(1), 201–222, 10.1093/gji/ggac247.

Giammarinaro, B., Tsarsitalidou, C., & Hillers, G., 2024. Investigating the lateral resolution of the surface wave focal spot imaging technique using two-dimensional acoustic simulations, *Comptes Rendus. Géoscience*, 10.5802/crgeos.254.

Guéguen, P., Bard, P.-Y., & Chaévez-Garciéa, F. J., 2002. Site-City Seismic Interaction in Mexico City–Like Environments: An Analytical Study, *Bulletin of the Seismological Society of America*, **92**(2), 794–811, 10.1785/0120000306.

Heinecke, A., Breuer, A., Rettenberger, S., Bader, M., Gabriel, A., Pelties, C., Bode, A., Barth, W., Liao, X., Vaidyanathan, K., Smelyanskiy, M., & Dubey, P., 2014. Petascale High Order Dynamic Rupture Earthquake Simulations on Heterogeneous Supercomputers, in *SC14: Proceedings of the International Conference for High Performance Computing, Networking, Storage and Analysis*, pp. 3–14.

Hillers, G., Roux, P., Campillo, M., & Ben-Zion, Y., 2016. Focal spot imaging based on zero lag cross-correlation amplitude fields: Application to dense array data at the San Jacinto fault zone, *Journal of Geophysical Research: Solid Earth*, **121**(11), 8048–8067, 10.1002/2016JB013014.

Hillers, G., Bader, M., Boué, P., Campillo, M., Catheline, S., de Rosny, J., Gabriel, A.-A., Giammarinaro, B., Krenz, L., Lassas, M., et al., 2023. Resolution of elastic, anelastic, and anisotropic medium properties using surface wave focal spot imaging, in *AGU Fall Meeting Abstracts*, pp. S11B–04.

Igel, H., 2016. *Computational Seismology: A Practical Introduction*, Oxford University Press.

Innanen, K., 2018. Space-time boundary reflections in elastic media, *CREWES Research Report*.

Käser, M., Castro, C., Hermann, V., & Pelties, C., 2010. SeisSol – A Software for Seismic Wave Propagation Simulations, in *High Performance Computing in Science and Engineering, Garching/Munich 2009*, pp. 281–292, Springer Berlin Heidelberg, Berlin, Heidelberg.

Kiser, E. & Ishii, M., 2017. Back-projection imaging of earthquakes, *Annual Review of Earth and Planetary Sciences*, **45**, 271–299, 10.1146/annurev-earth-063016-015801.

Kopriva, D. A., Gassner, G. J., & Nordström, J., 2021. Stability of Discontinuous Galerkin Spectral Element Schemes for wave propagation when the coefficient matrices have jumps, *Journal of Scientific Computing*, **88**(1), 3, 10.1007/s10915-021-01516-w.

Krenz, L., Uphoff, C., Ulrich, T., Gabriel, A.-A., Abrahams, L. S., Dunham, E. M., & Bader, M., 2021. 3D acoustic-elastic coupling with gravity: the dynamics of the 2018 Palu, Sulawesi earthquake and tsunami, in *Proceedings of the International Conference for High Performance Computing, Networking, Storage and Analysis*, SC '21, Association for Computing Machinery, New York, NY, USA.

Krenz, L., Wolf, S., Hillers, G., Gabriel, A., & Bader, M., 2023. Numerical Simulations of Seismoacoustic Nuisance Patterns from an Induced M 1.8 Earthquake in the Helsinki, Southern Finland, Metropolitan Area, *Bulletin of the Seismological Society of America*, **113**(4), 1596–1615, 10.1785/0120220225.

Krüger, F. & Ohrnberger, M., 2005. Tracking the rupture of the mw = 9.3 sumatra earthquake over 1,150 km at teleseismic distance, *Nature*, **435**(7044), 937–939, 10.1038/nature03696.

Käser, M. & Dumbser, M., 2006. An arbitrary high-order discontinuous Galerkin method for elastic waves on unstructured meshes — I. The two-dimensional isotropic case with external source terms, *Geophysical Journal International*, **166**(2), 855–877, 10.1111/j.1365-246X.2006.03051.x.

Käser, M., Hermann, V., & Puente, J. d. l., 2008. Quantitative accuracy analysis of the discontinuous galerkin method for seismic wave propagation, *Geophysical Journal International*, **173**(3), 990–999, 10.1111/j.1365-246X.2008.03781.x.

Larmat, C., Montagner, J.-P., Fink, M., Capdeville, Y., Tourin, A., & Clévédé, E., 2006. Time-reversal imaging of seismic sources and application to the great Sumatra earthquake, *Geophysical Research Letters*, **33**(19), 10.1029/2006GL026336.

LeVeque, R. J., 2002. *Finite Volume Methods for Hyperbolic Problems*, Cambridge Texts in Applied Mathematics, Cambridge University Press.

Lewy, H., Friedrichs, K., & Courant, R., 1928. Über die partiellen differenzengleichungen der mathematischen physik, *Mathematische Annalen*, **100**, 32–74.

Lin, F.-C., Ritzwoller, M. H., & Snieder, R., 2009. Eikonal tomography: surface wave tomography by phase front tracking across a regional broad-band seismic array, *Geophysical Journal International*, **177**(3), 1091–1110, 10.1111/j.1365-246X.2009.04105.x.

McMechan, G. A., 1982. Determination of source parameters by wavefield extrapolation, *Geophysical Journal International*, **71**(3), 613–628, 10.1111/j.1365-246X.1982.tb02788.x.

Mendonça, J. & Shukla, P., 2002. Time refraction and time reflection: two basic concepts, *Physica Scripta*, **65**(2), 160.

Moczo, P., Ampuero, J., Kristek, J., Galis, M., Day, S., & Igel, H., 2006. The European network SPICE code validation, vol. 8, Geophysical Research Abstracts, Abstract 1607-7962/gra/EGU06-A-05760.

Mu, D., Shu, H., Zhao, L., & An, S., 2020. A review of research on seismic metamaterials, *Advanced Engineering Materials*, **22**(4), 1901148, https://doi.org/10.1002/adem.201901148.

Pacheco-Peña, V. & Engheta, N., 2020. Antireflection temporal coatings, *Optica*, **7**(4), 323–331, 10.1364/OPTICA.381175.

Palgunadi, K. H., Gabriel, A.-A., Garagash, D. I., Ulrich, T., & Mai, P. M., 2024. Rupture dynamics of cascading earthquakes in a multiscale fracture network, *Journal of Geophysical Research: Solid Earth*, **129**(3), e2023JB027578, https://doi.org/10.1029/2023JB027578, e2023JB027578 2023JB027578.

Pendry, J. B., 2008. Time reversal and negative refraction, *Science*, **322**(5898), 71–73, 10.1126/science.1162087.

Peng, D., Fan, Y., Liu, R., Guo, X., & Wang, S., 2020. Time-reversed water waves generated from an instantaneous time mirror, *Journal of Physics Communications*, **4**(10), 105013.

Pilz, M., Roux, P., Mohammed, S. A., Garcia, R. F., Steinmann, R., Aubert, C., Bernauer, F., Guéguen, P., Ohrnberger, M., & Cotton, F., 2024. Wind turbines as a metamaterial-like urban layer: an experimental investigation using a dense seismic array and complementary sensing technologies, *Frontiers in Earth Science*, **12**, 10.3389/feart.2024.1352027.

Pu, X. & Shi, Z., 2020. Broadband surface wave attenuation in periodic trench barriers, *Journal of Sound and Vibration*, **468**, 115130, 10.1016/j.jsv.2019.115130.

Rietbrock, A. & Scherbaum, F., 1994. Acoustic imaging of earthquake sources from the Chalfant Valley, 1986, aftershock series, *Geophysical Journal International*, **119**(1), 260–268, 10.1111/j.1365-246X.1994.tb00926.x.

Roux, P., Bindi, D., Boxberger, T., Colombi, A., Cotton, F., Douste-Bacque, I., Garambois, S., Guéguen, P., Hillers, G., Hollis, D., Lecocq, T., & Pondaven, I., 2018. Toward Seismic Metamaterials: The METAFORET Project, *Seismological Research Letters*, **89**(2A), 582–593, 10.1785/0220170196.

Shapiro, N. M., Campillo, M., Stehly, L., & Ritzwoller, M. H., 2005. High-Resolution Surface-Wave Tomography from Ambient Seismic Noise, *Science*, **307**(5715), 1615–1618, 10.1126/science.1108339.

Taufiqurrahman, T., Gabriel, A.-A., Li, D., Ulrich, T., Li, B., Carena, S., Verdecchia, A., & Gallovič, F., 2023. Dynamics, interactions and delays of the 2019 ridgecrest rupture sequence, *Nature*, **618**(7964), 308–315, 10.1038/s41586-023-05985-x.

Tirole, R., Vezzoli, S., Galiffi, E., Robertson, I., Maurice, D., Tilmann, B., Maier, S. A., Pendry, J. B., & Sapienza, R., 2023. Double-slit time diffraction at optical frequencies, *Nature Physics*, **19**(7), 999–1002, 10.1038/s41567-023-01993-w.

Titarev, V. A. & Toro, E. F., 2002. ADER: Arbitrary high order Godunov approach, *J. Sci. Comput.*, **17**(1–4), 609–618, 10.1023/A:1015126814947.

Tromp, J., Tape, C., & Liu, Q., 2005. Seismic tomography, adjoint methods, time reversal and banana-doughnut kernels, *Geophysical Journal International*, **160**(1), 195–216, 10.1111/j.1365-246X.2004.02453.x.

Tsarsitalidou, C., Hillers, G., Giammarinaro, B., Boué, P., Stehly, L., & Campillo, M., 2024. Long period rayleigh wave focal spot imaging applied to usarray data, *Journal of Geophysical Research: Solid Earth*, **129**(5), e2023JB027417, https://doi.org/10.1029/2023JB027417.

Uphoff, C. & Bader, M., 2016. Generating high performance matrix kernels for earthquake simulations with viscoelastic attenuation, in *2016 International Conference on High Performance Computing Simulation (HPCS)*, pp. 908–916.

Uphoff, C. & Bader, M., 2020. Yet Another Tensor Toolbox for Discontinuous Galerkin Methods and Other Applications, *ACM Transactions on Mathematical Software*, **46**(4), 34:1–34:40, 10.1145/3406835.

Uphoff, C., Rettenberger, S., Bader, M., Madden, E. H., Ulrich, T., Wollherr, S., & Gabriel, A.-A., 2017. Extreme Scale Multi-physics Simulations of the Tsunamigenic 2004 Sumatra Megathrust Earthquake, in *Proceedings of the International Conference for High Performance Computing, Networking, Storage and Analysis*, SC '17, pp. 21:1–21:16, ACM, New York, NY, USA.

Wapenaar, K., Aichele, J., & van Manen, D.-J., 2024. Waves in space-dependent and time-dependent materials: A systematic comparison, *Wave Motion*, **130**, 103374, 10.1016/j.wavemoti.2024.103374.

Wolf, S., Gabriel, A.-A., & Bader, M., 2020a. Optimization and local time stepping of an ader-dg scheme for fully anisotropic wave propagation in complex geometries, in *Computational Science - ICCS 2020*, no. 12139 in Lecture Notes in Computer Science, pp. 32–45, Springer.

Wolf, S., Gabriel, A.-A., & Bader, M., 2020b. Optimization and Local Time Stepping of an ADER-DG Scheme for Fully Anisotropic Wave Propagation in Complex Geometries, in *Computational Science – ICCS 2020*, Lecture Notes in Computer Science, pp. 32–45, Springer International Publishing, Cham.

Wolf, S., Galis, M., Uphoff, C., Gabriel, A.-A., Moczo, P., Gregor, D., & Bader, M., 2022. An efficient ADER-DG local time stepping scheme for 3D HPC simulation of seismic waves in poroelastic media, *Journal of Computational Physics*, **455**, 1–29, 10.1016/j.jcp.2021.110886.

Wu, C. T., Nobre, N. M., Fort, E., Riley, G. D., & Costen, F., 2022. Tailoring Instantaneous Time Mirrors for Time Reversal Focusing in Absorbing Media, *IEEE Transactions on Antennas and Propagation*, **70**(10), 9630–9640, 10.1109/TAP.2022.3184482.